DNMT1-Mediated Regulation of Somatostatin-positive Interneuron Migration Impacts Cortical Architecture and Function

Authors:

Julia Reichard[1,2*], Philip Wolff[1,2*], Song Xie[3,4], Ke Zuo[3,5,6], Camila L. Fullio[7,8], Jian Du[1], Severin Graff[2,9], Jenice Linde[1,2], Can Bora Yildiz[1,2], Georg Pitschelatow[1,2], Gerion Nabbefeld[2,10], Lilli Dorp[1], Johanna Vollmer[1], Linda Biemans[1], Shirley Kempf[1], Minali Singh[11], K. Naga Mohan[11], Chao-Chung Kuo[12], Tanja Vogel[7], Paolo Carloni[3,4], Simon Musall[2,9] and Geraldine Zimmer-Bensch[1, 2]

* equal contribution

These authors contributed equally: Julia Reichard, Philip Wolff

Affiliations

[1] RWTH Aachen University, Division of Neuroepigenetics, Institute of Zoology (Biology 2), Worringerweg 3, 52074 Aachen, Germany.

[2] Research Training Group 2416 MultiSenses – MultiScales, RWTH Aachen University, 52074 Aachen, Germany

[3] Institute of Neuroscience and Medicine (INM-9) Computational Biomedicine, Forschungszentrum Jülich GmbH, 52428 Jülich, Germany

[4] RWTH Aachen University, Department of Physics, 52074 Aachen, Germany

[5] College of Pharmacy (International Academy of Targeted Therapeutics and Innovation), Chongqing University of Arts and Sciences, 402160 Chongqing, PR China

[6] Department of Physics, University of Cagliari, I-09042 Cagliari, Italy

[7] Institute for Anatomy and Cell Biology, Department of Molecular Embryology, Faculty of Medicine, Albert-Ludwigs-University Freiburg, 79104 Freiburg, Germany

[8] Faculty of Biology, Albert-Ludwigs-University Freiburg, 79104 Freiburg, Germany

[9] Institute of Biological Information Processing (IBI-3) Bioelectronics, Forschungszentrum Jülich, Germany

[10] RWTH Aachen University, Division of Neurophysiology, Institute of Zoology (Biology 2), Worringerweg 3, 52074 Aachen, Germany.

[11] Molecular Biology and Genetics Laboratory, Department of Biological Sciences, BITS Pilani, Hyderabad Campus, Hyderabad, India

[12] Genomics Facility, Interdisciplinary Center for Clinical Research (IZKF), RWTH Aachen University, 52074 Aachen, Germany

Abstract

The fine-tuned establishment of neuronal circuits during the formation of the cerebral cortex is pivotal for its functionality. Developmental abnormalities affecting the composition of cortical circuits, which consist of excitatory neurons and inhibitory cortical interneurons (cINs), are linked to a spectrum of neuropsychiatric disorders. Excitatory neurons originate in cortical proliferative zones, while inhibitory interneurons migrate from discrete domains of the basal telencephalon into the cortex. This migration is intricately governed by intrinsic genetic programs and extrinsic cues. Our current study reveals the role of the DNA methyltransferase 1 (DNMT1) in regulating the expression of key genes implicated in mouse cIN development

and in guiding the migration of somatostatin (SST)- expressing interneurons at postmitotic level within the developing cortex. *Dnmt1* deletion causes SST+ cINs to exit prematurely from the superficial migratory stream. In addition to the perturbed migration pattern and altered gene expression signatures, *Dnmt1*-deficient SST+ cINs had a discernible non-cell autonomous effect on cortical progenitors, which culminated in nuanced alterations of layer thicknesses in the adult cortex. Our study uncovers that DNMT1 governs the migration of SST+ cINs and through this, their instructive role in sculpting the intricate cortical layer architecture by signaling to cortical progenitors, with pronounced effects on neuronal network function.

Introduction

The intricate neuronal circuitry of the mammalian cerebral cortex, composed of excitatory and inhibitory neurons, empowers its enormous cognitive capabilities. The circuit formation involves coordinated developmental steps: proliferation, differentiation, migration, morphological maturation, and synapse formation[1].

Excitatory cortical projection neurons originate from radial glial cells (RGCs) and intermediate progenitors (IPCs) located in the cortical proliferative zones, through direct and indirect neurogenesis. Symmetric divisions of RGCs initially expand the progenitor pool, later shifting to asymmetric divisions to produce neurons and RGCs or IPCs[2;3]. EOMES-expressing IPCs localize to the subventricular zone (SVZ) and generate neurons for all cortical layers after few self-renewal divisions[3]. Cortical excitatory neurons are produced in a time-dependent manner, with deep-layer neurons born first and later-born neurons forming superficial layers, coming with unique functional features and connectivity[4]. Cortical neuron generation is modulated by both intrinsic and extrinsic factors[2;3]. Intrinsic mechanisms include (epi)genetic factors that dictate the developmental potential of progenitors. Extrinsic factors encompass signaling molecules from neighboring cells, postmitotic neurons in the cortical plate (CP), embryonic cerebrospinal fluid secreted by the choroid plexus, and incoming thalamic afferents[5–9]. These signals influence the timed self-renewal and neurogenic potential of cortical progenitors. Additionally, invading cortical inhibitory interneurons (cINs) have been proposed to influence EOMES+ IPCs, thereby impacting the proper formation of cortical layers[10].

Despite composing only 10-20% of the neuronal population, cINs, including Parvalbumin (PV) and somatostatin (SST) interneuron subtypes, are pivotal for precise information processing by inhibiting both excitatory and other inhibitory neurons[11]. Disturbing their development impairs the balance between excitation and inhibition, leading to abnormal cortical activity and cognitive impairments associated with various neurological and neuropsychiatric disorders, including schizophrenia and epilepsy[12–15]. The different types of cINs originate in three subpallial structures: the medial ganglionic eminence (MGE), the caudal ganglionic eminence (CGE), and the preoptic area (POA)[11]. The MGE gives rise to PV+ and SST+ interneurons, whereas the CGE generates Serotonin 3A receptor (5HTR3a) subtypes[16,17]. The POA produces mostly neurogliaform cells and Neuropeptide Y (NPY) expressing multipolar interneurons[18,19]. Postmitotic cINs migrate tangentially through the basal telencephalon into the cortex[13]. They invade the developing cortex along the marginal zone (MZ) and SVZ/intermediate zone (IZ), where they spread tangentially before switching to radial migration to enter the CP. This migration is guided by a diverse array of intrinsic and extrinsic cues[13,20–23]. For example, the transcription factors ARX and LHX6, expressed in MGE-derived cINs,

directly and indirectly regulate the expression of cytokine receptors that mediate the attraction to CXCL12, which is expressed in the MZ migratory route of the developing cortex[24,25]. After tangentially spreading over the cortical areas, cINs invade the cortical plate. The cortical plate expresses NRG2, which exerts attractive effects on ERBB4-expressing interneurons[26].

Epigenetic mechanisms, including histone modifications and DNA methylation, modulate intrinsic transcriptional programs[15,27]. It was previously reported that the DNA methyltransferase 1 (DNMT1) regulates gene expression in post-mitotic POA-derived cINs, promoting their proper migration and survival through non-canonical interactions with histone modifications[28]. Post-mitotic MGE-derived cINs, which give rise to SST$^+$ and PV$^+$ interneuron subtypes, also express DNMT1[28]. However, DNMT1 function in these subsets of immature, migrating cINs is unknown as of yet.

SST-expressing cells constitute about 30% of all cINs and play vital roles in inhibitory control, network synchronization, circuit plasticity, and cognitive functions[29]. SST$^+$ cINs encompass two main subtypes: Martinotti cells, which migrate along the marginal zone (MZ) during development and form axon collaterals in layer I, and non-Martinotti cells, which disperse via the SVZ/IZ and have different layer distributions as well as targeting properties[13,29].

The distinct migratory paths of SST$^+$ interneurons are regulated by ARX and LHX6, as well as MAFB[24,30,31]. Specifically, MAFB marks Martinotti cells and, along with ARX and LHX6, directs their migration along the MZ[24,30,31]. This migration is closely associated with the subsequent formation of axonal arbors in layer I[31].

Recognizing the functional relevance of SST$^+$ cINs in cortical circuitry and the necessity of their precise development for cortical function, we investigated the role of DNMT1 in this process. Addressing this gap in knowledge advances the understanding of cell type-specific epigenetic regulation in cortical network formation.

Our findings show that reduced *Dnmt1* expression in SST$^+$ cINs disrupts the transcriptional and DNA methylation profiles of key genes for cIN development, such as *Arx*, altering their migration along the MZ. This misregulation impacts excitatory cortical progenitor dynamics, affecting neurogenesis, and cortical layering, ultimately leading to functional and behavioral abnormalities in adulthood.

Results

Molecular dynamics simulations propose DNMT1´s catalytic domain binding to unmethylated DNA

DNMT1 is described as a maintenance methyltransferase, preserving DNA methylation during replication. This view is largely based on the comparison between a cryo-EM structure, showing a binding of DNMT1's catalytic domain to the hemimethylated oligo 5′-ApCpTpTpApCpGpGpApApGpGp-3' (HDNA)[32], and the X-ray structure of the unmethylated oligo 5'- TpCpCpCpGpTpGpApGpCpCpTpCpCpGpCpApGpGp-3' (UMDNA), which reveals weaker binding[33]. The latter observation is in apparent contrast to the reported dissociation constant (K_d) of the DNMT1/UMDNA complex in aqueous solution in the nM range[34], comparable to that of DNMT1/HDNA and other high-affinity DNA/protein complexes (**Extended Data Table E1**). Together with recent findings reporting DNMT1 expression and functions in postmitotic and even adult neurons, such as POA and MGE-derived cortical GABAergic interneurons[28,35–37], this proposes DNMT1 to have enzymatic functions in neurons other than the methylation of HDNA.

136 Visual inspection of the X-ray structure[33] suggests that the weak interactions between the
137 UMDNA and the catalytic domain of DNMT1 are caused by additional intermolecular contacts
138 of UMDNA with two surrounding DNMT1 molecules in the crystal lattice **(Fig. 1a, Extended**
139 **Figure E1a-f)**. Consistently, in three independent 500-ns-long molecular dynamics (MD)
140 simulations in solution, in conditions similar to those used for the K_d measurements[34] (details
141 are provided in **Extended data Tables 1-5**, and the **Supplementary methods**), the two
142 moieties undergo a significant rearrangement at the end of the dynamics. Almost all of the
143 interactions of the UMDNA's 5' region are formed with the catalytic domain, which performs
144 the enzymatic reaction (**Fig. 1b-g, Extended Data Fig. E1g and h**). A CpG moiety interacts
145 with Arg1234 and Asn1236 (**Fig. 1c**), as seen also in the cryo-EM structure of the
146 HDNA/DNMT1 complex[32] (PDB ID: 7XI9, **Extended Data Table E2**). The number of contacts
147 between the protein and UMDNA in solution, which lacks the additional DNMT1 molecules that
148 are present in the crystal **(Fig. 1a, b)**, increased about 60% compared to the crystal structure
149 (**Fig. 1d-g, Extended Data Fig. E1g, h**). Bioinformatic analysis showed that the solution MD
150 structure aligns with other DNA/protein complexes with affinities in the nM range: the number
151 of contacts for A^2 of contact surfaces is 0.17, which is comparable to other complexes ranging
152 from 0.17 to 0.21 (**Extended Data Table E1**). Thus, DNMT1 binds to UMDNA in solution
153 stronger than in the crystal phase because of packing forces, consistent with K_d measurements
154 in solution[34].
155 Our analysis supports DNMT1's broader functional role beyond maintenance methylation
156 including potential DNA methylation-dependent regulation in postmitotic, non-replicating
157 neurons, if the MD simulations reproduce the *in vivo* conditions.
158
159 **DNMT1 regulates key genes governing cIN development in embryonic SST$^+$ cells**
160 To examine the role of DNMT1 in SST$^+$ cIN development, we generated a conditional knockout
161 (KO) mouse model, in which *Dnmt1* deletion is induced by *Cre*-expression in postmitotic SST$^+$
162 cells (*Sst-Cre/tdTomato/Dnmt1 loxP*^{2}). *Sst-Cre/tdTomato* mice served as controls (**Extended**
163 **Data Fig. E2a**). The *Sst-Cre* deleter strain is a well-established model, with *Cre*-dependent
164 tdTomato expression being evident as cells leave the MGE (**Fig. 2b, c**), consistent with other
165 studies[38–40]. Validation of the mouse models is shown in **Extended Data Fig. E2b-n**.
166 We focused on embryonic day (E) 14.5, a critical stage characterized by extensive SST$^+$ cIN
167 migration through the basal telencephalon and the onset of tangential migration within the
168 cerebral cortex[41]. To identify putative DNMT1 target genes, we conducted RNA sequencing
169 and methyl-sequencing of FACS-enriched E14.5 *Sst-Cre/tdTomato/Dnmt1 loxP*^{2} (*Dnmt1* KO)
170 and *Sst-Cre/tdTomato* (control) cells from the basal telencephalon. We revealed 1,160
171 differentially expressed genes (DEGs) and 13,080 differentially methylated regions (DMRs)
172 overlapping annotated genomic regions (**Fig. 1h-j, Supplementary Table 1, 2**). Correlating
173 DMRs with the DEGs, we identified 600 genes exhibiting both transcriptional alterations and
174 DNA methylation changes in *Dnmt1* KO cells (**Fig. 1j, Supplementary Table 1-3**). Consistent
175 with previous findings[28,36], we observed up- or downregulated genes, as well as DMRs
176 showing gain and loss in DNA methylation upon *Dnmt1* deletion. This aligns with findings from
177 others, demonstrating that reduced *Dnmt1* and *Dnmt3a* expression leads to both gene
178 activation and repression[38,42]. Downregulated genes are often interpreted as indirect effects,
179 for instance, resulting from *Dnmt1* deletion-induced upregulation of a transcriptional
180 repressor or adaptive transcriptional responses to physiological changes[36,38,42]. Given the

181 partially redundant functions of DNMT1 and DNMT3A[43], compensatory DNMT3A activity may
182 contribute to the increased DNA methylation levels observed after *Dnmt1* deletion
183 (**Supplementary Table 2**).
184 To identify potential targets of DNMT1-dependent repressive DNA methylation, we focused on
185 the 349 of the 600 genes, which were upregulated in *Dnmt1* KO samples and displayed DMRs
186 (**Fig. 1j**). Notably, 66 of these 349 genes contained DNMT1 binding motifs that we identified
187 through additional ChIP-sequencing experiments (**Fig. 1j, k, Supplementary Table 4**).
188 Gene ontology (GO) enrichment analysis of upregulated genes with altered DNA methylation
189 in *Dnmt1* KO cells revealed an overrepresentation of genes associated with nervous system
190 development, neuron differentiation, cell-cell signaling, locomotion, neurogenesis, and cell
191 differentiation (**Fig. 1m, Extended Data Fig. E3a; Supplementary Table 5)**. A similar
192 enrichment was observed for the entire set of significantly upregulated genes in *Dnmt1* KO
193 cells, regardless of concurrent DNA methylation changes (**Extended Data Fig. E3d,**
194 **Supplementary Table 6**). Notably, many genes upregulated in E14.5 *Dnmt1* KO samples
195 were downregulated in embryonic stem cell (ESC)-derived *Dnmt1*$^{tet/tet}$ neurons overexpressing
196 DNMT1[44], highlighting DNMT1's repressive role in neurodevelopmental gene regulation (**Fig.**
197 **1l, Supplementary Table 7, 8**). Moreover, DNMT1-regulated genes in SST^{+} cINs exhibited
198 significantly longer coding sequences, transcript lengths, genome spans, and extended 3′ and
199 5′ UTRs compared to the entire set of genes detected in SST^{+} cINs (*Chi-squared test*;
200 **Extended Data Fig. E3b, c, e, f and E4b, c**). This aligns with the observation that *Mecp2*
201 deletion, a reader of DNA methylation[45], similarly leads to the upregulation of long genes
202 expressed during neurodevelopment[46].
203 Among DEGs with increased expression and DMRs in *Dnmt1* KO cINs, we identified genes
204 coding for key cortical interneuron differentiation and maturation regulators, including *Arx*,
205 *Zeb2*, *Mef2c*, *Dlx5*, *Sox6*, *Maf*, *Mafb*, and *Lhx6* (**Fig. 1h, i**). In addition to these well-
206 characterized transcription factors governing cIN fate and migration[13,41,47], DNMT1 also
207 regulated genes impacting locomotion, and cell-cell signaling (**Fig. 1h, i).** These included
208 *Erbb4*, *Reln*, *Robo2*, and members of the Eph/ephrin family such as *Efnb2*, all of which encode
209 proteins critical for directional guidance and neuronal positioning[26,48,49,50].
210 From these upregulated genes, *Erbb4*, *Arx*, *Zeb2*, *Maf*, and *Mafb* exhibited reduced DNA
211 methylation, with *Erbb4*, *Arx*, and *Zeb2* showing the most pronounced reduction in DNA
212 methylation averaged across all DMRs per gene (**Fig. 1i**). Of note, *Dnmt1* deletion in E14.5
213 SST^{+} cINs resulted in DMRs near transcriptional start sites (TSS) as well as within intragenic
214 regions and intergenic loci (**Supplementary Table 2**). Given that promoter DNA methylation
215 typically correlates with transcriptional repression[51], we further examined methylation changes
216 at the TSS of key cIN genes dysregulated in both *Dnmt1* KO and in *Dnmt1* overexpressing
217 neurons (**Fig. 1n**; **Supplementary Table 7**). For *Arx*, *Zeb2*, *Mafb*, and *Sox6* reduced DMRs
218 appeared at or near TSSs (**Fig. 1n, o**), aligning with their elevated expression in E14.5 *Dnmt1*
219 KO cells (**Fig. 1h, i**). *Erbb4* exhibited intragenic DMRs more distant from the TSS
220 (**Supplementary Table 2**). Intragenic DNA methylation has diverse regulatory functions, but
221 is particularly implicated in neuronal differentiation and migration[52,53]. Consistently, many
222 dysregulated genes in E14.5 *Dnmt1* KO samples encode proteins essential for cIN
223 development and migration, such as ARX[24], ZEB2[54,55] and ERBB4[26]. In sum, our findings
224 suggest that DNMT1 establishes proper gene regulatory networks essential for proper
225 migration and differentiation of cortical SST^{+} interneurons.

226
227 ***Dnmt1* deletion in postmitotic SST⁺ interneurons causes a premature exit from the**
228 **superficial migratory stream in the embryonic cortex**
229 To investigate the potential impact of DNMT1 on SST⁺ cIN migration, we next analyzed brain
230 sections of *Sst-Cre/tdTomato/Dnmt1 loxP²* (*Dnmt1* KO) and *Sst-Cre/tdTomato* (control)
231 embryos. We initially focused on E14.5, when first SST⁺ interneurons have reached the
232 cerebral cortex (**Fig. 2a-c**). Cortical dimensions were analyzed to confirm that both genotypes
233 were at the same developmental stage (**Extended Data Fig. E5a, b**). *In situ* examination of
234 *tdTomato*-expressing cells in E14.5 coronal brain sections revealed overall comparable
235 numbers of SST⁺ cINs in the cortex and the basal telencephalon in both genotypes (**Fig. 2d,**
236 **e**), indicating that the migration to the cortex was not impaired. However, within the cortex, we
237 observed a reduced proportion of *tdTomato* cells migrating along the MZ and a significant
238 increase of cells within the cortical plate (CP) in *Dnmt1* KO brain sections (**Fig. 2f-i**). Live-cell
239 imaging of organotypic brain slices at E14.5 for 20 hours confirmed an elevated fraction of
240 *Dnmt1* KO cells that deviated from the superficial migratory stream and entered the CP (**Fig.**
241 **2j-q, Supplementary Movies 1 and 2**). Notably, *Dnmt1* KO cells displayed a significantly
242 increased frequency of directional changes compared to control *Sst-Cre/tdTomato* cells (**Fig.**
243 **2m**), suggesting a disruption in their ability to remain confined along the superficial migratory
244 stream within the MZ. Moreover, their migratory pace was enhanced, which was particularly
245 evident for radially migrating cells, and cells migrating through the CP **(Fig. 2n, o; Extended**
246 **Data Fig. E6a**). This aligns with an increased path length seen for the migrating *Dnmt1* KO
247 cells in living brain slices (**Extended Data Fig. E6b**). Of note, in contrast to *Dnmt1*-deficient
248 POA-derived *Hmx3*-expressing interneurons[28], we did not observe morphological
249 abnormalities for migrating *Sst-Cre/tdTomato/Dnmt1 loxP²* cells (**Extended Data Fig. E6c**).
250 Consistently, *in vitro* experiments aiming to assess the morphology of *Dnmt1* siRNA-treated
251 MGE cells (E14.5 + 1DIV) did not reveal detectable morphological differences compared to
252 control conditions (**Extended Data Fig. E6d-g**).
253 Given the impaired migration within the cerebral cortex, we profiled the transcriptional changes
254 underlying the premature exit of SST⁺ interneurons from the marginal zone and their increased
255 invasion of the CP in E14.5 *Dnmt1* KO embryos. To this end, we conducted RNA sequencing
256 on FACS-enriched *Sst-Cre/tdTomato* cells isolated from the E14.5 cortex of both genotypes
257 (**Fig. 2r-t, Supplementary Table 9**). Notably, we obtained a prominent overlap with the
258 upregulated genes identified in *Dnmt1* KO cells from the basal telencephalon, with master
259 regulators of GABAergic interneuron differentiation and migration such as *Dlx1*, *Dlx2*, *Dlx5*,
260 *Arx*, *Lhx6*, *Maf*, *Mafb*, *Mef2c*, *Satb1*, and *Zeb2* being altered in expression in both datasets
261 (**Fig. 2r, s, t**). Of note, *Mef2c,* known to be regulated by *Maf* and *Mafb,* is a key factor in
262 specifying PV⁺ cINs[56]. Similarly, *Dlx5* is implicated in PV⁺ cIN development[57].
263 Also, genes related to cell-cell signaling appeared significantly overrepresented among the
264 commonly upregulated genes in *Dnmt1* KO cells from both compartments (**Fig. 2t,**
265 **Supplementary Table 9**). This included *Erbb4* (**Fig. 2r, s, Extended Data Fig. E6h, i**), known
266 to facilitate cIN invasion into the cortical plate upon activation by its ligand Neuregulin 3
267 (NRG3)[26]. Its increased expression could thus mediate the premature exit of *Dnmt1* KO cells
268 from the superficial migratory stream.
269 Additionally, *Efnb2* expression was persistently elevated in *Dnmt1* KO cells upon entering the
270 cortex. Since EPHB1 is strongly expressed in the cortical MZ[20] and acts as a repulsive cue for

271 migrating neurons from the basal telencephalon via reverse signaling[58], the
272 increased *Efnb2* levels could promote further the premature exit from the MZ.
273 Together, these findings emphasize that DNMT1 is critical for regulating the proper
274 development and migration of SST+ cINs within the cortex at E14.5, acting through control of
275 key genes involved in cIN migration and differentiation.
276 Although *Dnmt1*-deficient SST+ interneurons prematurely invaded the CP by E14.5 within 20
277 hours (**Fig. 2j-l**), we did not observe significant differences at later developmental stages
278 (E16.5 and E18.5). This was neither the case for the proportion of cells that reached the cortex
279 nor for the absolute number, density, or distribution of *Dnmt1* KO cells within the cortical
280 regions quantified (**Extended Data Fig. E7**). The cortical dimensions were likewise similar
281 between knockout and wildtype embryos at E16.5 and E18.5 (**Extended Data Fig. E5c-f**),
282 confirming that the embryos analyzed were of comparable developmental stages. This
283 suggests that the impact of *Dnmt1* deletion on the directional migration of SST+ cINs within the
284 MZ may be transient.
285
286 **DNMT1-dependent regulation of SST+ interneuron migration affects cortical progenitors**
287 **non-cell-autonomously**
288 The development of cINs and cortical excitatory neurons is intricately linked[10,59], and
289 supernumerary cINs in the IZ elicit altered IPC numbers impacting the generation of upper-
290 layer excitatory neurons[47]. Observing an impaired migration pattern of SST+ cINs prematurely
291 invading the CP and proliferative zones prompted us to investigate its influence on excitatory
292 cortical progenitors and neurogenesis. Moreover, we found changed expression of genes
293 involved in cell-cell signaling, known to modulate cortical neurogenesis, such as *EfnB2*[60], in
294 *Dnmt1* KO cells. EFNB2 binds to EPHA4[61], which is expressed in RGCs[5]. Activation of EPHA4
295 receptors by EFNA5, imported by invading thalamic afferents, has been shown to regulate
296 RGC division, impacting IPC generation and cortical layer formation[5].
297 To investigate whether the altered migration pattern and/or expression of signaling molecules
298 in *Dnmt1* KO embryos affects the generation of cortical excitatory neurons, we performed
299 immunostaining for TBR1, labeling early-born neurons of the preplate and layer VI[62,63]. We
300 found a significant increase in TBR1+ cell numbers within the CP in E14.5 *Dnmt1* KO brains
301 (**Fig. 3a-c**), which became even more evident at E16.5 (**Fig. 3f-h**). At E18.5 the radial
302 extension of both layer VI (TBR1+ cells) and the remaining CP were significantly expanded in
303 the conditional *Dnmt1* KO embryos compared to age-matched controls (**Fig. 3k-m, p and q**).
304 We next investigated potential changes in EOMES+ IPCs in *Dnmt1* KO embryos, which
305 represent an intermediate progenitor stage from RGCs to neurons, proposed to give rise to
306 most cortical projection neurons of all cortical layers[64;65,66], and had already been reported to
307 be impacted by cINs[10]. Consistently, we observed an increase in EOMES+ IPCs at E14.5 (**Fig.**
308 **3d, e**) and E16.5 (**Fig. 3i, j**) in *Dnmt1*-deficient embryos, coinciding with the timing of the
309 premature exit of *Dnmt1*-deficient SST+ interneurons from the MZ at E14.5 and the elevated
310 numbers of TBR1+ neurons. As no differences in the pool of IPCs were detected at E18.5 (**Fig.**
311 **3n, o**), the deletion of *Dnmt1* therefore seems to elicit a temporally restricted non-cell
312 autonomous effect on cortical IPCs and the production of deep-layer neurons.
313
314 **DNMT1 function in SST+ interneurons modulates cortical progenitor and neurogenesis**

The non-cell-autonomous effects of *Dnmt1* deletion in SST+ cINs on cortical progenitors and the increased generation of deep-layer neurons suggest that SST+ interneurons provide signaling cues influencing progenitor dynamics, similar to thalamic afferents importing EFNA5[5]. Notably, altered expression of signaling molecules known to modulate cortical neurogenesis and progenitor division, including *Wnt7a* and *EfnB2* (**Figure 2s, t, Supplementary Table 1, 9**)[6, 60,69] were detected in *Dnmt1* KO cells.

To further investigate potential cIN-progenitor interactions, we employed CellChat analysis of scRNA-sequencing data from E14.5 dorsal telencephalon, predicting ligand-receptor interactions between SST+ cINs and cortical progenitor types: RGCs and IPCs (**Fig. 4a, b, Extended Data Fig. E8a-c**).

NRXN3-NLGN1 signaling had the highest probability for interactions between SST+ cINs with both RGCs and IPCs. However, *Nrxn3* was not detected among the upregulated genes in *Sst-Cre/tdTomato/Dnmt1 loxP*[2] cINs at E14.5 (**Supplementary Table 9**). In addition, EFNB2-EPHA4 signaling was revealed as a potential mediator of these interactions, with *EfnB2* expressing SST+ MGE-interneurons interaction with RGCs as well as IPCs at E14.5 (**Fig. 4a, b**). E16.5 scRNA-sequencing data from the dorsal telencephalon retrieved similar results (**Extended Data Fig. 8d, e**). Supporting this, *Efnb2* was upregulated in *Dnmt1*-deficient SST+ cINs and altered in *Dnmt1*-overexpressing neurons (**Fig. 1h, Fig. 2s, t; Supplementary Table 1, 7, 9**). Given its known role in promoting neurogenesis at mid-corticogenesis[60] and its known binding to EPHA4[69] being expressed by RGCs[5], we hypothesized that increased *Efnb2* expression in *Dnmt1*-deficient SST+ cINs contributes to enhanced RGC differentiation into IPCs and deep-layer neurons. Pair-cell assays confirmed that ephrinB2-Fc stimulation promotes neurogenic RGC divisions and IPC generation (**Fig. 4c-f**).

To examine altered cIN-progenitor interactions in *Dnmt1* KO embryos, we performed single-nucleus (sn) RNA-seq on E16.5 cortical cells from both genotypes. This approach allowed sample freezing for simultaneous processing and captured potential differences in cIN-progenitor interactions but also non-cell-autonomous effects on postmitotic neuron generation, which might become more pronounced at this developmental stage.

Aligning with the histological data, *Dnmt1* KO samples at E16.5 showed an increased proportion of deep-layer cortical neurons and a reduced fraction of upper-layer neurons (**Fig. 4g-l; Extended Data Fig. 8f, h, i**). Additionally, *Erbb4*, *Arx*, and *Maf* - key regulators of cIN development - along with numerous other genes previously identified as upregulated through bulk RNA sequencing of E14.5 cortical *Dnmt1* KO cells, displayed significantly elevated expression in *Sst*+/*Gad2*+ cells from the E16.5 *Dnmt1* KO samples (**Extended Data Fig. 8g**). Applying *CellChat* analysis, genotype-related differences in interactions between MGE interneurons (senders) and RGCs were revealed, while this was not evident for the interaction between MGE interneurons and IPCs (numbers and interaction strength; **Fig. 4k, l**). This supports the instructive role of cINs on RGCs, and that this influence was increased in *Dnmt1* KO embryos. We further conducted MERFISH analysis in E16.5 brain sections of *Sst-Cre/tdTomato/Dnmt1 loxP*[2] and *Sst-Cre/tdTomato* embryos. Here, we also confirmed the elevated proportion of deep-layer neurons in *Dnmt1* KO brains and an increase in IPCs **(Fig. 4 m, n, o; Extended Data Figure 9)**.

In summary, DNMT1 is crucial for migration and function of SST+ cINs, with its loss disrupting migration trajectories, altering signaling, and promoting RGC differentiation into IPCs and deep-layer neurons.

360
361 ***Dnmt1* deletion-induced changes at embryonic stages manifest in an altered cortical**
362 **architecture at adult stages**
363 Finally, we investigated whether the *Dnmt1* deficiency-related embryonic defects results in
364 long-lasting structural changes in the adult cortex. We conducted a comparative analysis of
365 the distribution, density, and fate of *Sst-Cre/tdTomato* control and *Dnmt1* KO interneurons in
366 cortices of adult mice. Immunohistochemistry confirmed SST expression *Sst-Cre/tdTomato*
367 cells, as well as the reported co-expression of NPY and CALB2 (Calretinin)[70] in both genotypes
368 (**Extended Data Fig. E10a-e**). However, the proportion of SST$^+$ cINs co-expressing PV[71] was
369 significantly increased in *Dnmt1* KO mice compared to controls (**Extended Data Fig. E10e-j**).
370 This is in line with the elevated transcription of *Dlx5* and *Mef2c* found in E14.5 *Dnmt1* KO cells
371 (**Fig 1h, i; Fig. 2t**), both coding for drivers of PV$^+$ cINs development[57,72,73].
372 *Sst-Cre/tdTomato* cIN numbers were comparable across all layers between genotypes (**Fig.**
373 **5a-c**), but cell density in the superficial layers was significantly increased in *Dnmt1* KO mice
374 **(Fig. 5c)**. This correlated with a reduced radial extension of CUX1-positive layers II-IV and an
375 expansion of deep layers V-VI, while overall cortical thickness remained unchanged **(Fig. 5a,**
376 **b, d).**
377 The shift in layer proportions aligns with increased TBR1$^+$ neurons and IPCs at E14.5 and
378 E16.5, as well as snRNA-seq and MERFISH findings (Fig. 3, 4). These results indicate that
379 *Dnmt1* deletion in SST$^+$ interneurons non-cell autonomously alters cortical progenitor
380 dynamics, impacting adult cortical architecture and SST$^+$ cIN densities in superficial layers.
381
382 ***Sst-Cre/tdTomato/Dnmt1 loxP^2* mice display functional abnormalities**
383 To determine whether the observed structural alterations in the adult cortex also translate into
384 functional changes, we conducted electrophysiological recordings in the primary
385 somatosensory barrel cortex (S1) of awake head-fixed *Dnmt1* KO and control mice on a
386 running wheel (**Fig. 5e left**, **Extended Data Fig. E11**). To simultaneously capture population
387 and single-cell neural activity across the entire cortical depth, we recorded with high-density
388 Neuropixels probes (**Fig. 5e right; Extended Data Fig. E11a, b**) while mice were passively
389 stimulated with short air puffs to their whisker pad[74]. Tactile stimulation induced a clear
390 transient response in average local field potentials (LFPs) in S1 of control mice, whereas LFP
391 responses in conditional *Dnmt1* KO mice were much weaker and temporally delayed
392 (**Extended Data Fig. E11c**). To dissect the spatiotemporal structure of neural responses
393 across all cortical layers, we employed a current source density (CSD) analysis based on our
394 LFP recordings[75]. Consistent with the structural alterations in *Dnmt1* KO cortices, we found
395 clear differences in responses across layers between the genotypes. As expected from the
396 literature[76], the earliest responses for control mice (**Fig. 5f left**) occurred in the granular layer
397 (~400 μm cortical depth), then spreading to layer II/III (100-300 μm) and layer V (500-900 μm),
398 which indicates intact spatiotemporal processing of sensory signals. In contrast, the CSD
399 profile of *Dnmt1* KO mice was severely disrupted, with tactile responses being largely confined
400 to the deeper infragranular layers and only weak responses in the superficial layers (**Fig. 5f**
401 **right**). Quantification of CSD peak responses across the entire depth confirmed that the most
402 pronounced differences between *Dnmt1* KO and control mice occurred in the upper cortical
403 layers (**Fig. 5g, h**). Notably, while control mice exhibited a positive rebound following the initial

404 negative CSD deflection, the responses in *Dnmt1* KO mice lacked this feature, possibly due to
405 disrupted feed-forward inhibition (**Fig. 5h**).
406 To quantify the tactile responses of cortical S1 neurons, we also used spike-sorting to isolate
407 the spiking activity of sorted clusters. Consistent with our earlier results, the average spiking
408 activity of S1 neurons showed that tactile responses were much weaker in *Dnmt1* KO mice,
409 especially in the superficial layers (**Fig. 5i**, **Extended Data Fig. E11d**). Moreover, spiking
410 responses of upper-layer neurons were much longer lasting compared to controls, with neural
411 activity extending up to 400 ms after stimulation. This suggests reduced temporal precision in
412 sensory processing in *Dnmt1* KO mice, potentially due to impaired feedback inhibition.
413 We also investigated whether functional alterations manifest at the level of cortical network
414 oscillations. Gamma (γ) oscillations from 30-120 Hz, which strongly rely on the accurate
415 function of SST$^+$ cINs[77,78], are essential for integrating neural networks within and across brain
416 structures during cognitive processes, and abnormalities are a feature of cognitive diseases
417 such as schizophrenia, Alzheimer's disease, and Fragile X syndrome[79]. Thus, changes in γ-
418 oscillations represent a useful marker of function and dysfunction in cortical circuit
419 operations[80]. Indeed, the high-frequency LFP power in S1 was significantly reduced in *Dnmt1*
420 KO versus control animals (**Fig. 5j left**).
421 Similar disruptions in oscillatory network dynamics were observed in the primary visual cortex
422 (V1; **Fig. 5j right**). Visual stimulation (5-s-long visual grating stimuli) reliably induced
423 γ-oscillations in V1, with control mice showing a clear 70 Hz peak, consistent with stimulus-
424 induced γ activity (Fig. 5k, l). This effect was markedly reduced in *Dnmt1* KO mice, which
425 instead exhibited increased low-frequency activity in superficial cortical layers **(Fig. 5k, l)**.
426 These oscillatory changes suggest that *Dnmt1* deletion disrupts neural networks, likely due to
427 structural alterations in cortical architecture, particularly in superficial layers.
428 To distinguish whether these functional deficits stem from altered cortical structure or impaired
429 SST$^+$ cIN function, we optogenetically activated SST$^+$ cINs and assessed their spontaneous
430 firing, action potential waveform, and inhibitory capacity **(Extended Data Fig. E11d-g)**. No
431 significant differences emerged between control and *Dnmt1* KO neurons, indicating that SST$^+$
432 cIN functionality remained intact. Thus, the observed cortical network disruptions likely result
433 from structural changes, such as superficial layer thinning and increased SST$^+$ cIN density,
434 rather than a generalized impairment of SST$^+$ cIN function.
435
436 ***Sst-Cre/tdTomato/Dnmt1* KO mice display behavioral abnormalities**
437 To investigate whether functional impairments in *Dnmt1* KO mice translated into impaired
438 behavior we tested the animals' sensory perception. Therefore, we employed a visuo-tactile
439 evidence accumulation task and trained head-fixed *Dnmt1* KO and control mice to detect
440 tactile and visual stimuli. Both genotypes learned the stimulus detection at similar rates,
441 performed both uni- and multisensory task conditions with equal behavioral performances and
442 showed multisensory enhancement (**Extended Data Fig. E12a-d**), indicating intact sensory
443 perception in *Dnmt1*-deficient mice. Moreover, we tested learning and memory capabilities
444 using the Morris water maze, which also showed no differences between genotypes
445 (**Extended Data Fig. E12e-g**).
446 Notably, we observed abnormal eye movements in head-fixed *Dnmt1* KO mice during the tests
447 on the running wheel, characterized by brief episodes of significantly dilated pupils (more than
448 double their normal size) lasting 30-60 seconds, accompanied by facial spasms or salivation

449 (**Fig. 6a**). These episodes of pupil dilation correlated with a marked increase in low-frequency
450 activity (1–4 Hz), indicating epileptiform activity in KO mice (**Fig. 6b**). Further analysis of the
451 propagation of this activity across cortical depth revealed that these events were particularly
452 prominent in the superficial layers (**Fig. 6c**). In line with this, we detected prolonged seizure
453 durations for *Dnmt1* KO ² mice in response to administration of PTZ (pentylenetetrazol), which
454 is widely utilized to examine epileptic events in animal models and to assess changes in
455 seizure responses[81] (**Figure 6d-f**, **Supplementary Videos 3-9**). The latencies to the first
456 occurrence of various epileptic events were comparable between genotypes (**Extended Data**
457 **Fig. 12h, i**). However, *Dnmt1*-deficient mice exhibited higher Racine scale scores[82], indicating
458 increased seizure severity (**Figure 6d-f)**. This aligns with studies reporting that alterations in
459 SST⁺ cIN activity and function can lead to epileptic events[83] and γ oscillations have also been
460 proposed to play a role in seizure generation[84].
461 Moreover, we observed frequent repetitive motor behavior of *Dnmt1* KO mice in their home
462 cages (**Supplementary Video 10**). Such behavioral abnormalities are often linked to
463 neurological and neuropsychiatric diseases[85]. Notably, seizures frequently co-occur with
464 comorbid symptoms, including autism-like stereotypies (e.g., repetitive motor behavior) and
465 mood disorder-related phenotypes[86]. Thus, we next assessed nest-building performance, as
466 this test assessed behavior associated with neuropsychiatric disorders[87]. In line with our
467 functional results, we found that *Dnmt1* KO mice showed a reduced performance in nest-
468 building and diminished interest in the provided nest-building material (**Fig. 6g-j**).
469 In summary, our cellular, functional, and behavioral results demonstrate that *Dnmt1* deletion
470 in postmitotic SST⁺ interneurons leads to altered cortical architecture and network function in
471 adult mice, manifesting in disease-related behavioral abnormalities. This strongly suggests
472 that DNMT1 plays a crucial role in the development of SST⁺ interneurons and has non-cell
473 autonomous functions essential for the proper formation of the cerebral cortex.
474
475 **Discussion**
476 Two novel and main features of cortical development arise from our experiments: (i) dispersion
477 of SST⁺ interneurons along the superficial migratory stream within the cortical MZ is regulated
478 by DNMT1, and (ii) invading cINs influence RGCs and thereby proper cortical layering.
479 *Dnmt1* deletion in SST-expressing interneurons caused a premature exit from the MZ at E14.5,
480 accompanied by increased numbers of EOMES⁺ IPCs at E14.5, and more TBR1-positive
481 postmitotic neurons at E14.5 and E16.5, likely resulting from an altered division mode of RGCs.
482 This led to an increased generation of deep-layer neurons and enlarged deep layers at adult
483 stages, while upper layers were reduced in radial extension. These changes in cortical
484 architecture together with altered densities of SST⁺ interneurons in adult mice were associated
485 with prominent functional and behavioral deficits, demonstrating the importance of DNMT1 for
486 establishing accurate network function in the adult cortex.
487
488 While DNMT1 is well known as a maintenance methyltransferase, primarily responsible for
489 preserving DNA methylation during replication, emerging evidence—including our findings—
490 suggests a broader role for DNMT1 in postmitotic neurons[35,36,43]. DNMT1 is expressed in non-
491 dividing POA- and MGE-derived cINs, where it is proposed to regulate neuronal development
492 through both canonical and non-canonical mechanisms[28,36]. Based on results in the crystal
493 phase, Song et al[33] have suggested weak binding of DNMT1's catalytic domain to UMDNA.

494 Solution-based affinity measurements challenge this hypothesis, demonstrating a high-affinity
495 interaction for both HDNA/DNMT1 and UMDNA/DNMT1 complexes[34], that is in similar scale
496 compared to other DNA-protein complexes. Our MD simulations resolve this contradiction by
497 showing that UMDNA undergoes a significant conformational rearrangement in solution,
498 increasing the interactions of its CpG sites with DNMT1's catalytic domain, as it was observed
499 for the HDNA/DNMT1 complex[32]. Given that our findings in solution are valid also for *in vivo*
500 conditions, they support the hypothesis that DNMT1 has a functional role beyond maintenance
501 methylation. In line with this, DNMT1 has been shown to interact with CFP1 (CysxxCys finger
502 protein 1), which presents a high affinity for unmethylated DNA[88]. Moreover, *de novo*
503 methylation activity at certain repetitive elements and single copy sequences has already been
504 shown for DNMT1[89]. Functional cooperation of DNMT1 during *de novo* methylation of DNA
505 has further been described[90], and gene-specific *de novo* methylation can be initiated by
506 reintroduction of DNMT1 in cells lacking DNMT1 and DNMT3b, that present with nearly absent
507 genomic methylation[91]. Taken together, these observations strongly propose DNMT1´s
508 function beyond maintenance DNA methylation, likely contributing to (*de novo*) DNA
509 methylation-dependent gene regulation in postmitotic neurons. This provides an additional
510 layer of epigenetic control during neuronal differentiation and function. In combination with its
511 described non-canonical actions through crosstalk with histone-modifying mechanisms[28,92],
512 our findings render DNMT1 as an active participant in epigenetic programming in postmitotic
513 cINs and putatively also other neuronal subsets[35,36,43].
514
515 *Dnmt1* deletion in SST$^+$ cINs impairs their migration within the MZ. Martinotti cells, constituting
516 the majority of SST$^+$ interneurons[70], migrate primarily along the MZ during corticogenesis[31],
517 while non-Martinotti SST$^+$ cells disperse rather via the SVZ/IZ[31]. Given the selective effects of
518 *Dnmt1* deletion on MZ migrating SST$^+$ interneurons, DNMT1 seems to be relevant for the
519 proper migration of Martinotti cells. Our global transcriptome and methylome analyses propose
520 that DNMT1 controls essential key transcription factors of MGE cIN development such as
521 *Lhx6*, *Arx*, *Zeb2*, *Satb1*, *Sox6*, and *Dlx5*[13,41,47]. LHX6, ARX, MAF, and MAFB are proposed to
522 regulate the migration along the MZ, as *Lhx6*, *Maf*, *Mafb*, and *Arx* mutant mouse brains display
523 defects in MZ migration of cINs[24,30,31]. The altered expression of these genes in *Sst-*
524 *Cre/tdTomato/Dnmt1-loxP*[2] cells is in line with their premature exit from the MZ. For *Arx,* the
525 most prominent reduction in DNA methylation at the TSS was observed (**Fig. 1i, n**), which is
526 in line with its increased expression in *Sst-Cre/tdTomato/Dnmt1-loxP*[2] samples from the basal
527 telencephalon and the cortex. DNA methylation at promoter regions is well known for its
528 repressive power[51]. Thus, our data propose DNMT1 to keep proper *Arx* expression levels in
529 migrating SST$^+$ cINs, and through this regulate the migration along the MZ.
530 ARX has been reported to directly and indirectly modulate other genes controlling different
531 stages of cIN development, including *Maf*, *Mafb*, *Mef2c*, *Nkx2.1*, *Lmo1*, *Nrg1*, *Erbb4*, *Npr1*,
532 and *EphA4*[24], many of which were altered in expression upon *Dnmt1* deletion in SST$^+$
533 interneurons. For *Maf* and *Mafb*, we detected increased expression and reduced DNA
534 methylation levels in *Dnmt1* KO samples (**Fig. 1h, l, n**), pointing to a DNMT1-dependent
535 regulation as well. However, a transcriptional dysregulation of these and other ARX target
536 genes such as *Mef2c* or *Erbb4* as a secondary effect of changed *Arx* expression cannot be
537 excluded.

538 ERBB4 promotes the switch from tangential to radial migration and the distribution of
539 interneurons within the CP, by interacting with NRG3 being expressed in the CP[26]. As *Nrg3*
540 overexpression in the CP results in premature invasion of migrating interneurons into the CP[26],
541 the augmented *Erbb4* expression observed in *Sst-Cre/tdTomato/Dnmt1-loxP*[2] might cause the
542 premature exit from the MZ. Moreover, increased *efnB2* expression in *Sst-*
543 *Cre/tdTomato/Dnmt1-loxP*[2] cells could contribute to the precocious invasion of the CP. EPHB1
544 is expressed in the MZ[20], and EPHB1-triggered reverse signaling has already been shown to
545 elicit a repulsive response in migrating interneurons[58]. Of note, DNA methylation dependent
546 regulation of *efnB2* expression was already proposed in neuronal stem cells[93]. Thus, DNMT1-
547 mediated repression of *Erbb4* and *Efnb2* could regulate the proper migration of SST$^+$ cINs
548 along the superficial migratory stream and the timed invasion of the CP.
549 Apart from migration regulation, some of the dysregulated genes are involved in cell fate
550 determination of cINs. For example, MEF2C and DLX5 drive the PV fate[57,72,73], and both were
551 increasingly expressed in E14.5 *Sst-Cre/tdTomato/Dnmt1-loxP*[2] cells. MEF2C initiates distinct
552 transcriptional programs in immature PV$^+$ interneurons upon settling within the cortex by
553 opening the chromatin landscapes at PV-specific loci[72,73]. In addition to ARX, MAF, and MAFB,
554 promote *Mef2c* expression[56], which also increased in expression upon *Dnmt1* deletion. This
555 aligns with the rise in PV-positive SST$^+$ tdTomato cINs in adult *Dnmt1* KO mice. Thus,
556 alongside migration regulation, DNMT1-dependent transcriptional remodeling seems to
557 promote the SST$^+$ cIN cell fate. Thus, although bulk RNA and methyl sequencing of FAC-
558 sorted cells comes with limitations in matters of cell population heterogeneity, we obtained
559 transcriptional changes that align with the observed phenotype of disturbed migration along
560 the MZ, some of which were also confirmed by snRNA sequencing.
561 However, migration and final differentiation are interconnected processes. For example, the
562 migration of Martinotti cells is functionally related to the morphological maturation and thus,
563 the adaption of their final fate, as the proper formation of their axon collaterals in layer I
564 depends on their migration along the MZ[31]. These axon collaterals extend horizontally for up
565 to 2000 μm, making up approximately three-quarters (76%) of the GABAergic axons in this
566 layer[70]. This enables Martinotti cells to influence the activity of numerous pyramidal neurons,
567 which are their primary postsynaptic targets[70]. Hence, DNMT1 might also indirectly influence
568 the proper formation of these powerful axon collaterals in layer I, by promoting the migration
569 of SST$^+$ cINs along the MZ. Disturbed formation of axon collaterals could contribute to the
570 strong functional and behavioral impairments that we observed for adult *Sst-Cre/Dnmt1* KO
571 mice, despite the overall number of SST$^+$ cells not having been affected. This is consistent
572 with data from *Mafb* KO mice, which also display a premature exit from the MZ and no changes
573 in interneuron numbers and distribution in adults. Yet, functional impairments were likewise
574 observed[31].
575 The described functional deficits might also arise from the altered cortical architecture, which
576 seem to arise from the non-cell autonomous effect of *Dnmt1* deletion SST$^+$ cINs on cortical
577 progenitors, resulting in altered SST$^+$ cIN densities in the adult cortex, that link the effects on
578 migration to the adult phenotype.
579 SST+ cINs regulate cortical excitability and synchronization[70], for which their altered density in
580 the superficial layers of *Dnmt1* KO mice likely contributes to observed functional and
581 behavioral deficits. Consistently, functional impairments were most pronounced in these
582 layers. LFP recordings showed weaker, delayed tactile responses with disrupted

583 spatiotemporal processing, reduced activation, and prolonged spiking activity, particularly in
584 the upper layers. Alongside diminished γ-oscillations, low-frequency activity was increased.
585 Additionally, abnormal eye movements with severe pupil dilations correlated with heightened
586 low-frequency activity (1–4 Hz) in superficial layers, reinforcing the link between structural
587 changes and functional deficits.
588 As optogenetic stimulation revealed no intrinsic deficits in SST$^+$ cIN firing properties upon
589 *Dnmt1* deletion, our findings suggest that functional disruptions are primarily driven by
590 structural cortical alterations. However, we cannot exclude additional DNMT1-dependent
591 functional impairments in adult SST$^+$ cINs, akin to DNMT1's role in regulating GABAergic
592 transmission in PV interneurons[36]. Future studies using inducible *Sst-Cre/tdTomato/Dnmt1*
593 *loxP^2* mice to analyze methylation and gene expression signatures in adult SST$^+$ cINs could
594 clarify embryonic versus adult effects, though this is beyond the scope of the present study.
595
596 The expansion of deep cortical layers and reduction of upper layers observed in the adult
597 cortex in adult *Sst-Cre/tdTomato/Dnmt1 loxP^2* mice can be traced back to embryonic stages,
598 where enhanced deep-layer neuron production and altered IPC numbers were detected. This
599 strongly implies, that the migration defects in *Sst-Cre/tdTomato/Dnmt1 loxP^2* embryos non-
600 cell-autonomously affect cortical progenitors and hence the timed generation of cortical
601 neurons.
602 As evidenced by Sessa et al. (2010)[59], the development of cINs and excitatory neurons must
603 have been effectively integrated throughout evolution, since an increase in the production of
604 excitatory neurons also necessitates a rise in interneuron generation to maintain the proper
605 balance of excitation and inhibition. Moreover, invading cINs may influence cortical
606 progenitors, as they have been shown to modulate EOMES$^+$ IPC proliferation, thereby
607 affecting the timing of excitatory neuron generation[10]. Our findings extend this hypothesis by
608 providing evidence that cINs also impact RGCs, which in turn regulate IPC and neuronal
609 production.
610 Specifically, we implicate EFNB2-EPHA4 signaling in RGC division, similar to the reported
611 modulation of EPHA4-expressing RGCs by thalamic afferents importing EFNA5[5], which shifts
612 apical progenitors between proliferative and neurogenic divisions. Both EFNA5 and EphA4
613 deficiency enhances deep-layer neuron production by altering RGC neurogenic potential[5].
614 Similarly, cINs may provide external cues via membrane-bound or secreted signals. *Sst-*
615 *Cre/tdTomato/Dnmt1-loxP^2* interneurons showed increased *Efnb2* expression, encoding
616 EFNB2, a regulator of cortical neurogenesis. While progenitor-restricted *Efnb2* deletion delays
617 neurogenesis, EFNB2-driven EPHB signaling transiently boosts neuronal output[60], mirroring
618 our pair cell assay results. This ephrinB2-dependent neurogenic shift occurred within a specific
619 temporal window of corticogenesis[60], aligning with prior studies showing that temporally
620 restricted neurogenic changes shape cortical layer thickness[5,93].
621 In sum, the altered expression of secreted and membrane-bound signaling molecules with
622 known potential to regulate cortical progenitor division and fate, in concert with the altered
623 migration pattern of *Sst-Cre/tdTomato/Dnmt1 loxP^2* interneurons could lead to the defects in
624 cortical layer formation. This suggests an essential role for cINs in modulating the temporal
625 production of distinct subtypes of excitatory cortical neurons, and a high level of crosstalk
626 between immature cIN precursors and cortical progenitors to optimize the formation of neural

627 circuits. These findings also establish a key role for DNMT1 in orchestrating cortical
628 development through cell-autonomous and non-cell-autonomous actions.
629
630 **Methods:**
631
632 **Molecular Dynamics Simulations**
633 The AMBER 22 software suite was employed . Details on the DNMT1/UMDNA/SAM complex
634 and force field parameters are given in the **Extended data Figure E1 and Extended Data**
635 **Table E3-E5**. Long-range electrostatic interactions were calculated using the Particle Mesh
636 Ewald method[97]. Non-bonded interactions were treated with a 10 Å cutoff.
637 The system was energy-minimized *in vacuo* with 10,000 steps of steepest descent, followed
638 by 10,000 steps of conjugate gradient minimization in order to eliminate atomic collision. The
639 heavy-atom RMSD of the optimized configurations with respect to the initial geometry was
640 1.4 Å. Then, the complex was solvated in a truncated octahedral water box with a minimum
641 distance of 12 Å from the solute to the box edge (**Extended Data Table E5**). K^+, Na^+, and Cl^-
642 ions were added to neutralize the system. The concentration of K^+ was similar to that in the
643 nucleus (**Extended Data Table E5**). Periodic boundary conditions were applied. The whole
644 system was then subjected to (i) 10,000 steps of steepest descent followed by 10,000 steps
645 of conjugate gradient minimization with a 100 kcal/(mol·Å^2) restraint on the whole solute. (ii)
646 the same as (i), but with restraints only on heavy atoms of the solute; (iii) the same as (i), but
647 without restraints. Successively, the system was heated from 0 K to 100 K over 5 ps then
648 relaxed at 100 K for 5 ps, then from 100 K to 310 K in 0.5 ns, and finally relaxed at 310 K for
649 4.5 ns by using Langevin dynamics[98], with a restraint of 100 kcal/(mol·Å^2) was applied to the
650 heavy atoms of the solute. The time integration step was set to 1 fs. Finally, three independent
651 500 ns isobaric-isothermal simulations with different initial velocities were performed without
652 restraints and with a time step of 2 fs. Langevin dynamics[98] and the Monte Carlo barostat[99]
653 were used to maintain a constant temperature (310 K) and pressure (1 atm), respectively.
654 CPPTRAJ[100] was used for trajectory analyses.
655
656 **Animals**
657 In the recent study transgenic mouse strains with a genetic C57BL/6J background (initially
658 obtained from the University Hospital UKA Aachen, Germany) were used. *Sst*$^{tm2.l(cre)Zjh}$/J x
659 *B6.CgGt(ROSA)26Sor*$^{tml\ 4(\ CAG\text{-}tdTomato\ )Hze}$ (*Sst*$^{+/-}$*-Cre/tdTomato)* served as control animals
660 whereas *Sst*$^{tm2.l(cre)Zjh}$*/J* x B6.CgGt(ROSA)26Sor$^{tm14(CAG\text{-}tdTomato)Hze}$ x *B6; 129S-Dnmt1tm2Jae*/J
661 (*Sst-Cre*$^{+/-}$*/tdTomato/Dnmt1 loxP*^{2}*)* were used as *Dnmt1* knockout (KO) model. For more
662 details see supplementary information.
663
664
665 **Isolation of Embryonic and Adult Brains**
666 Individuals of embryonic stage 14.5, 16.5 or 18.5 were isolated as described in Symmank et
667 al. (2018)[101]. Briefly, pregnant females were anesthetized by intraperitoneal administration of
668 ketamine/xylazine (200/25 mg/kg living weight per injection up to a maximum application of
669 600/75 mg ketamine/xylazine per kg living weight in total). Upon reaching surgical tolerance,
670 the abdominal cavity was opened to expose the uterine horns that were removed. Embryos
671 were isolated from the uteri and decapitated. For histological analyses of E14.5 and E16.5

brains, the heads were directly transferred to 4% paraformaldehyde (PFA)/1x phosphate-buffered saline (PBS). For histological analyses at E18.5, brains were removed from the skull before transferring them to 4% PFA/1x PBS. E14.5 heads were fixed for 5 hours, while E16.5 heads and E18.5 brains were fixed overnight at 4 °C on an orbital shaker (50 rpm). Afterwards, stepwise cryopreservation was performed by overnight incubation first in 10% Sucrose/1x PBS, followed by 30% sucrose/1x PBS at 4 °C on an orbital shaker (50 rpm). Tissue was frozen in liquid nitrogen and stored at -80 °C.

For the isolation of adult brains, male mice were sacrificed with an overdose of 5% (v/v) isoflurane. For histological analyses and identification of Neuropixels recording sites, transcardial perfusion was conducted with 1x PBS (pH 7.4) followed by 4% PFA/1x PBS (pH 7.4) with a pump[102]. After brain preparation, post-fixation was conducted in 4% PFA/1x PBS for 24 h at 4°C on a roller mixer with constant rotation (approx. 50 rpm). Then, cryopreservation was performed in 10% sucrose/1x PBS and 30% sucrose/1x PBS for 24 h each at 4°C on a roller mixer with constant rotation (approx. 50 rpm) before brains were frozen in liquid nitrogen and stored at -80 °C.

Organotypic brain slices and single-cell preparations

MGE- and cortical single cells were prepared as described previously[20,36]. Briefly, embryonic heads were collected and dissected in Gey's Balanced Salt Solution (GBSS, pH 7.4)/0.65% D-glucose on ice. MGEs and cortices were cut out and collected in Hanks' Balanced Salt Solution (HBSS, w/ phenol red, w/o calcium, w/o magnesium)/0.65% D-glucose on ice. The tissue was treated with 0.04% of trypsin/EDTA (Thermo Fisher Scientific, U.S.A.) for 17 min at 37°C, before MGE cells were dissociated in cold Dulbecco's Modified Eagle Medium (DMEM) with additional L-glutamine and 4.5 g/L D-glucose (Thermo Fisher Scientific, U.S.A.), 10% fetal bovine serum (FBS; Biowest, U.S.A.), and 1% penicillin/streptomycin (P/S) (Thermo Fisher Scientific, U.S.A.) by trituration with glass Pasteur pipettes and by subsequent filtering through a nylon gauze (pore size 140 μm; Merck, U.S.A.). Dissociated single cells were seeded on laminin (19 μg/ml; Sigma-Aldrich, U.S.A.)/poly-L-lysine- (10 μg/ml; Sigma-Aldrich, U.S.A.) coated glass coverslips. For MGE cells, we used a density of 455 cells/mm^2. Cortical single cells were seeded in clonal densities of 150 cells/mm^2. Transfection of MGE cells with siRNA oligos occurred after 5–6 h of incubation (37°C, 5% CO_2 and 95% relative humidity) in Neurobasal medium with phenol red, 1x B27™, and 0.25x GlutaMAX (Gibco, U.S.A.) for 24 h. For this, the medium was supplemented with Lipofectamine™ 3000 in accordance with the manufacturer's instructions (Thermo Fisher, U.S.A.) together with *Dnmt1* siRNA (30 nM, #sc-35203, Santa Cruz, U.S.A.) and a scrambled control siRNA construct (15 nM, BLOCK-iT™ Fluorescent Oligo, #2013, Thermo Fisher, U.S.A.). After 24 h MGE cells were fixated with 4% PFA/1x PBS for 10 min.

Incubation of cortical cells plated at clonal density occurred at 37°C, 5% CO_2 and 95% relative humidity in culture medium (Neurobasal medium with phenol red, 1x B27™, 0.25x GlutaMAX (Gibco, U.S.A.), and 0.4% methylcellulose (Sigma, U.S.A.)) for 24 h. Treatment of cortical single cells was conducted 5–6 h after plating. For this, the medium was supplemented with 10 μM 5-ethynyl-2′-deoxyuridine (5-EdU, baseclick™, baseclick GmbH, Germany) and with either 5 μg/mL of a recombinant human Fc control protein (Rockland Immunochemicals, U.S.A.) or 5 μg/mL of a recombinant human efnB2-Fc (R&D Systems, U.S.A.). Both

717 recombinant proteins were pre-clustered with 10 μg/mL of an anti-human IgG antibody
718 (Thermo Fisher, U.S.A.). Cortical single cells were fixated with 4% PFA/1x PBS for 10 min.
719 For organotypic brain slice preparations[28], brains of E14.5 embryos were embedded in 4% low
720 melt agarose (37°C) in Krebs buffer (126 mM NaCl, 2.5 mM KCl, 1.2 mM NaH_2PO_4, 1.2 mM
721 $MgCl_2$ * $6H_2O$, 2.1 mM $CaCl_2$; pH 7.4; supplemented with 10 mM D-glucose and 12.5 mM
722 $NaHCO_3$, sterile-filtered). For sectioning of 350 μM coronal slices, a 5100mz-Plus vibrating
723 microtome (speed: 0.7–0.8 mm/s and blade oscillation frequency: 5 Hz; Camden Instruments,
724 United Kingdom) was used. Slices were transferred to ice-cold post-holding buffer (1x Krebs
725 buffer, 10 mM HEPES, 1% P/S, 0.2% gentamycin, pH 7.4). Slices were imaged in μ-slide 4
726 Well imaging plates (ibidi GmbH, Germany) coated with 19 μg/mL laminin (Sigma-Aldrich,
727 U.S.A.) and 10 μg/mL poly-L-lysine (Sigma-Aldrich, U.S.A.) in Neurobasal without phenol red,
728 1x B27™, 1% P/S, 0.5% D-glucose, 10 mM HEPES, using a confocal-like Leica DMi8
729 fluorescent microscope in combination with a THUNDER® imager unit (Leica, Germany) and
730 the corresponding software *LASX* (Leica, Germany) equipped with an incubation chamber
731 (37°C, 5% CO_2 and 95% relative humidity). Imaging was conducted with a wavelength of
732 544 nm (TRITC-channel) in tile scans including z-stacks of 8–10 μm step size every 15 min.
733 Post-processing of the respective footages was executed in the *LASX* software using the
734 "*Mosaic Merge*"- and "*Thunder Lightning (Large Volume)*"-tools. Finally, a maximum intensity
735 projection of the merged tile scans was processed using the *Fiji* software[103] and LASX.
736 Analysis was performed blindly using the manual track plugin from ImageJ (NIH, USA) to track
737 cells with a migration time of at least 6 h.
738
739 **Histology and immunocytochemistry**
740 For histology on embryonic brains, we used 50-μm coronal brain slices, cryosectioned with a
741 CM3050 S Cryostate (Leica, Germany), and collected on Superfrost®Plus (Avantor, U.S.A.)
742 object slides. On-slide immunohistochemistry was performed as described in Pensold et al.
743 (2017)[28]. Briefly, all samples were washed for 5x 20 min in 1x PBS /0.5% Triton X-100/0.5%
744 Tween®20 with constant horizontal shaking (50 rpm). After that, all samples were treated with
745 blocking solution (4% bovine serum albumin (BSA) and 10% normal goat serum in 1x
746 PBS/0.5% Triton X-100/0.5% Tween®20) was applied for 2 h at room temperature (RT).
747 Primary antibody incubation diluted in blocking solution was conducted overnight at RT in a
748 humid chamber. After washing for 5x 20 min in 1x PBS/0.5% Triton X-100/0.5% Tween®20,
749 secondary antibodies were applied in blocking solution for 2h at RT. After washing for 3 x 20
750 min, the samples were stained with 4',6-diamidino-2-phenylindol dihydrochloride (DAPI,
751 1:10000 in PBS, Carl Roth, Germany) for 15 min at RT, followed by washing twice for 5 min
752 with PBS, sections were embedded in Mowiol or Fluoromount (Thermo Fisher, U.S.A.).
753 For adult brains, immunohistochemistry was performed in free-floating sagittal and coronal
754 sections (30 μm), prepared using the CM3050 S Cryostate (Leica, Germany). Slices were
755 transferred to 1x PBS and stored at 4°C. For sagittal sections, Bregma 1.32 and 1.44 were
756 used, while Bregma 1.18, 1.10, 0.14, -0.22, -3.08, and -3.28 were taken for coronal sections.
757 The same procedure as for embryonic sections was applied, except that an antigen retrieval
758 with heated HistoVT One® (1x HistoVT One®/H_2O bidest., Nacalai, Japan) at 70°C for 20 min
759 was performed for staining against DNMT1. Sections that were stained for somatostatin,
760 calretinin, and NPY underwent an antigen retrieval with citrate buffer (95°C; 10 mM, pH 6.0,
761 supplemented with 0.5% Tween®20) for 15 min and subsequent cool-down for 30 min before

762 washing. Finally, all slices were transferred onto glass slides in 0.5% (w/v) gelatine/0.05%
763 (w/v) chromium(III) potassium sulfate dodecahydrate ($KCrS_2O_8$)/H_2O solution prior to
764 embedding in Mowiol.
765 Immunostaining on dissociated MGE and cortical single cells was conducted by washing
766 coverslips with 1x PBS/0.1% Triton X-100 for 3x 5 min and blocking with 1x PBS/0.1%
767 Triton X-100/4% BSA for 30 min at room temperature. Primary antibodies were applied for 2 h
768 at room temperature. After washing for 3x 5 min with 1x PBS/0.1% Triton X-100, the secondary
769 antibody was incubated for 1 h at room temperature. Phalloidin-647 diluted 1:1000 in 1x PBS
770 (#ab176759, Abcam, U.S.A.) was applied for 20 min after washing. Then a final washing step
771 with 1x PBS for 10 min and a DAPI staining (1:10000/1x PBS; Carl Roth, Germany) for 5 min
772 were performed and coverslips were mounted in Mowiol.

773 The following primary antibodies were used: mouse anti-Calretinin (1:500; Swant, Switzerland,
774 #6B3), rabbit anti-NPY (1:2500; Immunostar, U.S.A., #2940), rabbit anti-TBR1 (1:200; Abcam,
775 U.S.A., #ab31940); rabbit anti-EOMES (1:500; Abcam, U.S.A., #ab23345); rat anti-
776 Somatostatin (1:100; Millipore, U.S.A., #MAB354), mouse anti-Parvalbumin (1:2000; Swant,
777 Switzerland, #235); rabbit anti-DNMT1 (1:100; Santa Cruz, U.S.A., # sc20701); rabbit anti-
778 CUX1 (CDP; 1:100, Santa Cruz, U.S.A., #sc13024); mouse anti-Nestin (1:100; Merck U.S.A.,
779 #MAB353), rabbit anti-ß-Tubulin III (1:500; Sigma Aldrich, U.S.A., #T2200), and rabbit anti-
780 ErB4 (1:1000; Proteintech, U.S.A., #22387-1-AP).
781 The following secondary antibodies conjugated with respective fluorophores were used at
782 1:1000 dilutions: Alexa488-goat anti-Rat IgG (Invitrogen, U.S.A., #A11006) Cy5-Goat anti-
783 Rabbit IgG (Life Technologies, U.S.A., #A10523), A488-Donkey anti-Mouse IgG (Jackson,
784 U.S.A., #15454150), Cy5-Goat anti-Mouse IgG (Jackson, U.S.A., #115175146), A488-Goat
785 anti-Rabbit IgG (Life Technologies, U.S.A., #A11008).
786
787 **Transcriptome data on neurons overexpressing DNMT1**
788 *Dnmt1$^{tet/tet}$* mouse embryonic stem cells have been previously described[104]. The levels of
789 DNMT1 in these cells are four times higher than the normal wild-type *R1* ESCs. Upon
790 differentiation, the induced *Dnmt1$^{tet/tet}$* neurons produced contain twice the DNMT1 levels than
791 in *R1* neurons[104]. Differential expression gene data on *Tet/Tet* neurons was taken from Singh
792 *et al.* (2023)[44] and genes with significantly altered transcript levels were compared with the
793 transcriptome data on the tissues lacking DNMT1.
794
795 **Enrichment of E14.5 tdTomato cells for RNA and methyl-sequencing**
796 For FACS-mediated enrichment of *Sst-Cre/tdTomato* cells, telencephalons were prepared
797 from E14.5 embryos and subjected to cell dissociation. Nuclease-free reaction tubes were
798 used during isolation and long-term storage of the resulting material. The telencephalons were
799 collected in cold HBSS (w/ phenol red, w/o calcium, w/o magnesium)/0.65% D-glucose;
800 4 μg/μL (600 U) of DNAse I (AppliChem GmbH, Germany). After treatment with 0.04% trypsin
801 for 17 min at 37 °C, HBSS was replaced by DMEM with additional L-glutamine and 4.5 g/L D-
802 glucose, 10% FBS and 1% P/S to stop the trypsinization. Subsequently, the cells were
803 pelletized, resuspended and triturated in cold HBSS (w/o phenol red, w/o calcium, w/o
804 magnesium)/0.65% D-glucose, before being filtered through a nylon gauze (pore size 140 μm,
805 Merck, U.S.A.) for FACS.

806 FACS was performed by the Flow Cytometry Facility (FCF, University Hospital RWTH Aachen,
807 Germany). Respective parameters for the procedure using a BD FACS Aria Fusion (BD
808 Biosciences, U.S.A) were defined as follows: 5-laser (FCS, SSC, PE, BV421), 18-color (3-6-
809 2-4-3). TdTomato-positive cells were either collected in 100 μL of cold TRIzol™ (Thermo
810 Fisher Scientific, U.S.A.) for subsequent RNA sequencing or in 100 μL of cold HBSS (w/o
811 phenol red, w/o calcium, w/o magnesium)/0.65% D-glucose for further processing for DNA
812 methylation analysis. Finally, all samples were stored at -80 °C.
813
814 **Total RNA seq**
815 TdTomato-positive E14.5 *Sst-Cre/tdTomato or Sst-Cre/tdTomato/ Dnmt1 loxP*^{2} cells from the
816 basal telencephalon and the cortex were FAC sorted into 100 μL TRIzol™ reagent (Thermo
817 Fisher Scientific, U.S.A.). Samples were mixed by inversion and stored at -80 °C until
818 processing. RNA was isolated from 50,000 cells pooled per genotype. The samples were filled
819 up to 1 ml with TRIzol™ and dounced 25 times in a glass homogenizer using the small-
820 clearance pestle. Samples were incubated for 5 min at room temperature, supplemented with
821 200 μL chloroform, and mixed by shaking vigorously until a homogenous milky solution
822 appeared. Following another incubation at room temperature (until a visible phase separation
823 appeared) samples were centrifuged at 13,000x *g* and 4 °C for 15 min in a tabletop centrifuge
824 with cooling function. For precipitation, the clear upper phase was collected and mixed with
825 70% ethanol. Samples were bound onto RNeasy mini columns (Qiagen, Germany) and
826 washed according to the instructions in the manual. RNA was eluted with 30 μL nuclease-free
827 water.
828 RNA concentrations were determined using a Qubit™ 4 flourometer (Thermo Fisher Scientific,
829 U.S.A.) with RNA HS reagents (Thermo Fisher Scientific, U.S.A.). RNA integrity was checked
830 on a Tape Station 4200 using the HS RNA kit (Agilent Technologies, U.S.A.).
831 Prior to library preparation, samples were digested with HL dsDNAseI (ArcticZymes
832 Technologies ASA, Norway) for 10 min at 37 °C to remove traces of gDNA. To avoid digestion
833 of the newly generated cDNA during library preparation, the dsDNAseI was heat-inactivated
834 for 5 min at 58 °C. Thereafter, samples were subjected to library preparation using the
835 TAKARA SMARTer Stranded Total RNA-Seq Kit v3 - Pico Input Mammalian for Illumina
836 (Takara Bio, Japan). Fragmentation was done at 94°C for 4 min. Illumina adaptors and indices
837 were ligated to cDNA in a PCR reaction with 5 cycles (98 °C for 15 s, 55 °C for 15 s and 68 °C
838 for 30 s). RRNA depletion was performed on the amplified libraries. Final libraries were
839 subjected to an upscale PCR with 13 cycles (98 °C for 15 s, 55 °C for 15 s and 68 °C for 30
840 s). Amplified libraries were cleaned with magnetic AMPure XP beads (Beckman Coulter,
841 U.S.A.). Library concentration was determined with a Qubit™ 4 fluorometer using the 1x
842 dsDNA HS reagent (Thermo Fisher Scientific, U.S.A.). Library size was assessed on a Tape
843 Station 4200 using the DNA D1000 kit (Agilent Technologies, U.S.A.).
844 Libraries were diluted, equimolarly pooled, denatured, and loaded for clustering onto an
845 Illumina NovaSeq 6000 SP (200 cycles) flow cell (Illumina, U.S.A.) in conjunction with 1% PhiX
846 control library, and run on an Illumina NovaSeq machine (Illumina, U.S.A.) in 75 bp paired-end
847 mode. The 1% PhiX control library was spiked in to improve base calling accuracy.
848 *FASTQ* files were generated using *bcl2fastq* (Illumina, U.S.A.). To facilitate reproducible
849 analysis, samples were processed using the publicly available *nf-core/rnaseq* pipeline version
850 3.12[105] implemented in Nextflow 23.10.0[106] with minimal command. In brief, lane-level reads

were trimmed using *Trim Galore* 0.6.7[107] and aligned to the mouse genome (GRCm39) using *STAR 2.7.9a*[108]. Gene-level and transcript-level quantification was done by *Salmon v1.10.1*[109]. All analysis was performed using custom scripts in *R versi*on 4.3.2 using the *DESeq2 v.1.32.0* framework[110].

MethylSeq

TdTomato-positive E14.5 *Sst-Cre/tdTomato* and *Sst-Cre/tdTomato/ Dnmt1 loxP*[2] cells were FAC-sorted into 100 µL HBSS. Samples were mixed by inversion and stored at -80°C until processing.

DNA was isolated from at least 50.000 pooled cells per sample using the PureLink genomic DNA Mini Kit (Thermo Fisher Scientic, U.S.A.). Per genotype, the samples were initially pooled by volume (200 uL each), supplemented with lysis buffer provided in the kit and incubated with 2 µL proteinase K (Thermo Fisher Scientific, U.S.A.) at 55 °C for 10 min. DNA was precipitated with 100% ethanol. Samples were bound to one column per genotype each, washed as instructed, briefly dried and eluted with 35 µL Tris-EDTA (TE) buffer. DNA concentrations were determined using the Qubit™ 4 flourometer with the 1x dsDNA HS reagent (Thermo Fisher Scientic, U.S.A.). Quality/integrity was checked on a Tape Station 4200 using the Genomic DNA kit (Agilent Technologies, U.S.A.).

Libraries were generated using the Enzymatic Methyl-seq kit for Illumina (#E7120, New England Biolabs, U.S.A.). After enzymatic shearing for 25 min at 37 °C with the NEBNext UltraShear enzyme and buffer, followed by an inactivation at 65 °C for 15 min, 5-methylcytosines were oxidized by TET2 after adaptor ligation. Samples were denatured with formamide and deaminated with APOBEC. Libraries were subjected to 7 cycles of upscale PCR (98 °C for 10 s, 62 °C for 30 s, and 65 °C for 60 s). Library concentrations were determined with a Qubit™ 4 fluorometer and the 1x dsDNA HS reagent (Thermo Fisher Scientific, U.S.A.). All recommended clean-up steps were performed with magnetic AMPure XP beads (Beckman Coulter, U.S.A.). Library size was assessed on a Tape Station 4200 using the DNA D5000 kit (Agilent Technologies, U.S.A.). Concentrations were determined with a Qubit™ 4 fluorometer and the 1x dsDNA HS reagent (Thermo Fisher Scientific, U.S.A.).

Libraries were diluted, equimolarly pooled, denatured, and clustered onto an Illumina NextSeq 500/550 Mid Output Kit v2.5 (300 cycles) flow cell (Illumina, U.S.A.). The 1% PhiX control library was spiked in to improve base calling accuracy. Paired-end sequencing was performed with 151 cycles.

FASTQ files were generated using bcl2fastq (Illumina, U.S.A.). To facilitate reproducible analysis, samples were processed using the publicly available nf-core/methylseq pipeline version 2.6.0[105] implemented in Nextflow 23.10.0[106] with the minimal command. Briefly, FastQC (http://www.bioinformatics.babraham.ac.uk/projects/fastqc) and Trimmomatic[111] were utilized to perform quality control, and clean reads were aligned to the reference genome using Bismark[112] to account for bisulfite conversion and identify methylated cytosines. Differentially methylated sites and regions were called by the R package DSS[113] and annotated using the GENCODE VM23 dataset. Regions were similarly annotated with a margin of 1 kb in front of the TSS. Methylation tracks were converted from mm10 to mm39 using the USCS LiftOver tool[114] for integration with RNA seq data and visualized in IGV[115]. The sequence of the promoter regions (obtained from Ensembl release 112[116]) within these limits was further

896 analyzed for the enrichment of previously identified DNMT1-binding motifs using the AME
897 algorithm provided within the MEME suite[117]. Gene sets of interest were analyzed for the
898 enrichment of gene ontology terms using ShinyGO 0.80 with the biological processes'
899 dataset[118].
900
901
902 **Single-cell RNA-sequencing**
903 The dorsal telencephalons from E14.5 C57BL/6J mice were dissected. Single-cell
904 suspensions were prepared using a papain dissociation system (#LK003150; Worthington
905 Biochemical Corporation, U.S.A) and all centrifugation steps were done at 4°C. Cells were
906 manually counted using Trypan Blue exclusion, which consistently showed a viability greater
907 than 95%.
908 ScRNA-seq libraries were prepared using the 10x Genomics 3' Gene Expression Kit v3.1 (10x
909 Genomics, U.S.A). Each sample had a target of 10'000 cells and was independently loaded in
910 the Chromium Controller (10x Genomics, U.S.A). Quality control of the cDNA and final libraries
911 was conducted using the High Sensitivity RNA D5000 and D1000 ScreenTape assays (Agilent
912 Technologies, U.S.A.), respectively. Libraries were pooled and sequenced on a NovaSeq 6000
913 using the S2 Reagent Kit v1.5 with 100 cycles (Illumina, U.S.A).
914 *FASTQ* files were processed using *CellRanger v7.0.0*. All bioinformatics analysis was
915 performed in *R 4.4.0* running under *Ubuntu 20.04.6 LTS*. The *Seurat v5* package[119] was used
916 for filtering, quality control, clustering, and annotation of the data. *CellChat v2.1.2*[61] was used
917 to compute the cell communication probabilities among different clusters.
918
919 **Single-nucleus RNA-sequencing**
920 The medial neocortices from E16.5 *Sst-Cre/tdTomato* and *Sst-Cre/tdTomato/Dnmt1 loxP*[2]
921 mice were dissected. The samples were snap-frozen on dry ice and stored at -80 °C until
922 library preparation to ensure RNA integrity was maintained while the genotype and the sex of
923 each sample could be verified for a bias-free transcriptomic analysis. Consequently, single-
924 nucleus RNA sequencing (snRNA-seq) was selected over scRNA-seq to accommodate the
925 processing of frozen samples. The nuclei were extracted from the frozen tissue by
926 discontinuous sucrose gradient ultracentrifugation. Briefly, the tissue was homogenized in 1 ml
927 of lysis buffer (0.32 M sucrose, 10 mM Tris-HCl (pH 8.0), 5 mM CaCl2, 3 mM Mg acetate,
928 1 mM dithiothreitol (DTT), 0.1 mM EDTA, 0.1% Triton X-100, 50 U/ml RNase inhibitors
929 (#M0314S, New England Biolabs, U.S.A.)) using a 2-ml glass Dounce homogenizer on ice and
930 stroking 25 times with pestle A followed by 100 strokes with pestle B. The homogenates were
931 transferred to 5-ml ultracentrifuge tubes (#344057, Beckman Coulter) and under-layered with
932 3 ml of sucrose cushion (1.8 M sucrose, 10 mM Tris-HCl (pH 8.0), 3 mM Mg acetate, 1 mM
933 DTT, 50 U/ml RNase inhibitors). The samples were loaded onto a Sw-55 Ti rotor and
934 centrifuged for 1 h at 4 °C and 28,300 rpm (97,500x *g*). The nuclei pellets were resuspended
935 in 150 μl of cold 1% BSA in PBS and immediately fixed using the Evercode™ Nuclei Fixation
936 kit (Parse Biosciences, U.S.A.) following the manufacturer's guidelines. The fixed nuclei were
937 stored at -80 °C until library preparation.
938 The snRNA-seq libraries were generated with the Evercode™ WT kit (Parse Biosciences,
939 U.S.A.). The quality check of the cDNA and the final libraries was performed using the High
940 Sensitivity D5000 and D1000 ScreenTape kits (Agilent Technologies, U.S.A.). Libraries were

941 equimolarly pooled and sequenced in conjunction with 5% PhiX control library on an Illumina
942 NovaSeq machine in paired-end mode using the S2 Reagent Kit v1.5 (200 cycles) (Illumina,
943 U.S.A.).
944 The sequencing dataset was processed using the TrailmakerTM
945 (https://app.trailmaker.parsebiosciences.com/; Parse Biosciences, 2024). Unfiltered count
946 matrices were further processed using the Seurat package for R (R 4.4.1, Seurat
947 5.0.1.9001)[119]. Cells were filtered based on counts, discarding cells below 1500 and above
948 60000 reads per cell. Dead or dying cells were removed by filtering droplets with high
949 mitochondrial content (10% cut-off).
950 Subsequently data was normalized prior to principal-component analysis (PCA) and Leiden-
951 clustering. A Uniform Manifold Approximation and Projection (UMAP) embedding was
952 calculated to visualize the results. Cluster-specific marker genes were identified by comparing
953 cells of each cluster to all other cells using the presto package implementation of the Wilcoxon
954 rank-sum test. The top marker genes for each cluster were cross-referenced with known cell
955 type-specific markers from the literature and publicly available databases.
956 The Annotated Clusters were subsequently used to infer cell-cell communication probabilities
957 using the CellChat Database and corresponding R package (CellChat version 2.1.2)[61].
958
959
960 **MERSCOPE Analysis**
961 Spatial transcriptomic analysis was performed on 10 *µ*m brain sections from fresh-frozen
962 E16.5 *Sst-Cre/tdTomato* and *Sst-Cre/tdTomato/Dnmt1 loxP*[2] embryos using
963 the MERSCOPE™ system (Vizgen) according to the manufacturer's instructions. Briefly,
964 tissue samples were mounted onto specialized slides and fixed to preserve RNA
965 integrity. Multiplexed Error-Robust Fluorescence In Situ Hybridization (MERFISH) was then
966 applied, where gene-specific oligonucleotide probes hybridized to target RNA molecules. We
967 used the commercially available Pan Neuro panel covering 500 transcripts used for the
968 identification of cell types in the mouse Brain.
969 Following hybridization, high-resolution fluorescence imaging was conducted on the
970 MERSCOPE platform to capture the spatial distribution of individual transcripts at subcellular
971 resolution. The imaging data was preprocessed on the instrument, which decodes RNA
972 signals, assigns molecular identities, segments the tissue into cells and quantifies transcript
973 abundance across individual cells within the tissue.
974 Two brain tissue sections from comparable anatomical planes were analyzed using Seurat in
975 R *(R 4.4.1, Seurat 5.0.1.9001)*. After normalization and identification of highly variable features
976 for each dataset, the datasets were integrated using reciprocal PCA to account for shared
977 sources of variation. Clustering was performed using the Louvain algorithm at a resolution of
978 0.8, and clusters were manually annotated based on marker genes identified through
979 differential expression analysis. Heterogeneous clusters were further resolved through
980 subclustering, with iterative marker analysis and annotation revealing additional distinct cell
981 types and states within the brain tissue.
982
983 **Neuropixels recordings and behavioral experiments**
984 **Surgical Procedures**

985 Mice received systemic analgesia prior to surgical procedures in form of subcutaneous
986 injections of carprofen (4 mg/kg, Rimadyl, Zoetis GmbH, Germany) and buprenorphine
987 (0.1 mg/kg, Buprenovet sine, Bayer Vital GMBH, Germany) and were then anesthetized using
988 (1%–2.5%) isoflurane in oxygen. The eyes were covered with eye ointment (Bepanthen, Bayer
989 Vital GmbH, Germany) to prevent them from drying out. Following a local injection of
990 bupivacaine (0.08 ml of 0.25% Bucain 7.5mg/ml, Puren Pharma GmbH, Germany), the scalp
991 was incised and pushed outward to fix it in place using tissue adhesive (Vetbond, 3M). A
992 circular headbar was attached on top using dental cement (C&B Metabond, Parkell U.S.A.;
993 Ortho-Jet, Lang Dental). For electrophysiological recordings, craniotomies were performed to
994 inject a viral vector into the cortex (AAV1.shortCAG.dlox.hChR2(H134R).WPRE.hGHp, Zurich
995 Vector Core, viral titer = ~$8x10^{12}$ vg/ml). We targeted primary somatosensory (S1) and visual
996 (V1) cortex (stereotactic coordinates; S1: -1.5 mm anteroposterior and -3.5 mm mediolateral
997 from Bregma; V1: -4 mm anteroposterior and -2 mm mediolateral from Bregma) and injected
998 a volume of 200 nl in bouts of 10 nl with a 14-s delay between bouts (Nanoject III, Drummond
999 Scientific, U.S.A.). For each coordinate, injections were performed at two cortical depths (300
1000 and 600 μm), adding up to a total volume of 400 nl per injection site. The glass pipette was
1001 removed at least 5 min after the full volume was injected to reduce the risk of backflow. After
1002 viral injections a 3-mm wide round coverslip was placed inside the craniotomy and fixed with
1003 light-curable dental cement (DE Flowable composite, Nordenta, Germany). The coverslips
1004 contained a small opening (~0.2 mm) that was covered with silicon to allow access of the
1005 Neuropixels probes to the cortex. After the surgery, all animals received the same injections
1006 of carpofen and buprenorphine as in the beginning. They also received buprenorphine (0.009
1007 mg/ml, Buprenovet sine, Bayer Vital GmbH, Germany) and enrofloxacin (0.0227 mg/ml, Baytril
1008 5%, Bayer Vital GMBH, Germany) in their drinking water for three days following the surgery.
1009 Behavioral training started after at least two weeks of recovery
1010
1011 **Neuropixels recordings**
1012 Electrophysiological recordings were done with Neuropixels 1.0 Probes in head-fixed mice,
1013 freely running on a wheel. For each mouse, we performed four recordings on consecutive
1014 days. To later recover the probe position in each recording, the probes were painted with DiD
1015 cell labeling solution (Invitrogen V22887, U.S.A.) before each recording. To record neural
1016 responses to tactile stimulation across all cortical layers, the probes were inserted at an
1017 orthogonal angle to the brain surface (~10°). The stimulation protocol was started 5–10 min
1018 after insertion, we recorded high pass-filtered data above 300 Hz at 30 kHz and low pass-
1019 filtered signals between 0.5–100 Hz at 2.5 kHz from the bottom 384 channels of the
1020 Neuropixels probe (~3.8 mm active recording area). Signals were acquired with an external
1021 Neuropixels PXIe card (IMEC, Belgium) used in a PXIe-Chassis (PXIe-1071, National
1022 Instruments, USA). Triggers and control signals for different stimuli and wheel movements
1023 were separately recorded as analog and digital signals using the SpikeGLX software (Janelia
1024 Farm Research Campus, U.S.A.; Bill Karsh).
1025 Visual stimulation to induce gamma oscillations consisted of 5-s long full-field drifting square
1026 wave gratings at horizontal orientation and a spatial frequency of 0.04 cycles per degree. All
1027 visual stimuli were presented at a 17 cm distance from the right eye on a gamma-corrected
1028 LED-backlit LCD monitor (Viewsonic VX3276-2K-MHD-2, 32", 60Hz refresh rate). Tactile
1029 stimulation was controlled by a microcontroller-based finite state machine (Bpod r2, Sanworks,

U.S.A.) using custom Matlab code (2020b, MathWorks). Tactile stimuli consisted of 20-ms long air puffs at 0.03 bar pressure directed at the distal parts of the whiskers. In each trial, two air puffs were presented at an inter-stimulus interval of 500 ms. The overall stimulation protocol consisted of 50 tactile trials and 50 visual trials in randomized order. Inter-trial intervals were also randomized between 3–5 seconds.

To extract spiking activity, channels that were broken or outside of the brain were detected and removed from the recording using the SpikeInterface analysis toolbox. The remaining channels were time-shifted and median-subtracted across channels and time. Corrected channels were then spike-sorted with the Kilosort 2.5 software and manually curated using phy. All sorted spiking and local field potential data were analyzed using custom Matlab code (2020b, MathWorks).

Peri-event time histograms (PETHs) for sensory responses in each cluster were computed with a bin size of 10 ms and baseline-subtracted by the mean activity within 1 second before the laser onset (between 2 to 1 seconds before the first tactile stimulus). Trial-averaged local field potentials (LFPs) in response to sensory stimulation were similarly baseline-corrected. To compute current source densities (CSDs) from LFP signals, we used the inverse CSD method by Pettersen et al. (2006)[75]. We applied the spline iCSD method, assuming a smoothly varying CSD between electrode contacts, based on polynomial interpolation. We assumed a homogeneous, isotropic conductivity of $\sigma = 0.3$ S/m within and directly above the cortex[75]. To reduce spatial noise, the estimated CSD was subsequently convolved with a Gaussian spatial filter with a standard deviation of 0.1 mm. For LFP and CSD analyses, the signals from neighboring contacts at the same depth were averaged together to improve signal quality.

Evidence accumulation task

Head-fixed, water-deprived mice were stepwise introduced to performing a series of uni- or multisensory evidence accumulation tasks in a custom-built setup. The stimulus presentation, lick detection and reward delivery were driven by a microcontroller-based finite state machine running on a *Teensy 3.2* (PJRC) and using custom *Python* code (Python 3.7). For all trials, the general scheme of events was similar: for 3 seconds, randomized sequences of up to 6 visual, tactile or visuotactile stimuli were presented on one or both sides of the mouse. After a 0.5 s-long delay period, the animal had to respond within 2 seconds to obtain a reward. The ITI between trials was 3.5 seconds. Mice were first trained on reliably detecting visual stimuli, consisting of 6 visual gratings (spatial frequency = 0.018 cycles per degree) that were moving over the screen at a temporal frequency of 2 Hz. After mice learned to accurately respond on the side, where visual stimuli were presented, tactile stimuli were introduced in the form of 6 air puffs, as described above (see Neuropixels Recordings). Air puffs occurred at regular intervals of 0.5 seconds during the 3 second stimulus period. After mice also accurately detected the side of tactile stimulation, visuotactile stimuli were introduced where coherent visual and tactile stimuli were presented. Once mice achieved stable detection performances in all modalities, distractor stimuli of the same modality were introduced on the opposing side. While the number of stimuli in these trials varied to confront animals with different levels of difficulty, the general goal was for the mice to indicate the side with the higher number of presented stimuli.

Morris water maze (MWM)

1075 Visual navigation and learning capacities were investigated using a MWM. Mice were trained
1076 to search a translucent platform (Ø 10 cm) in a circular pool (Ø 1 m) containing tepid water.
1077 The pool was divided into four virtual quadrants, each of them equipped with distinct visual
1078 cues. Mice were tested on 6 consecutive days. Start positions for each trial were chosen at
1079 random. Mice remained on the platform for at least 5 s after finding it, to enable memorization
1080 of spatial cues. If a mouse did not find the platform within the given time limit, it was manually
1081 guided to the platform. In between trials, mice were kept underneath a red lamp for at least 10
1082 minutes. Animals were habituated to the task on their first day of experiments by performing
1083 four trials for a maximum duration of 90 seconds each. The translucent platform slightly
1084 protruded from the water surface to facilitate quick locating. On the following 5 training days,
1085 the platform was submerged 1-2 cm below the water surface. All animals conducted 12 trials
1086 per day with three starts per quadrant, respectively. The maximum duration per trial was set
1087 to 60 seconds. Mice were recorded from above and behavioral data were processed using
1088 ANY-maze (Stoelting Co., U.S.A).
1089
1090 **Nest-building procedure**
1091 Nest-shredding and -building tests were performed with male mice between 12 and 24 weeks
1092 of age. Both *Sst-Cre* strains were tested by placing respective animals in separate housing
1093 cages with ad libitum access to food and water but without further enrichment except for fresh
1094 bedding and nest-building material (standardized autoclaved nestlets with a weight of 2–3 g (5
1095 cm x 5 cm, Lexx, Germany). For each nestlet the weight was determined before the experiment
1096 which took place during the murine active phase (5 p.m. to 9 a.m.). After testing, all mice were
1097 transferred to their home cages and the percentual shredded material as well as the
1098 corresponding nest building score[95] were recorded. Mice were tested twice within one week
1099 with two days between both trials. The resulting data were averaged for each mouse.
1100
1101
1102 **Pentylenetetrazole (PTZ)-induced epileptic seizure protocol**
1103 Male *Sst-Cre/tdTomato* and *Sst-Cre/tdTomato/Dnmt1 LoxP*^{2} mice (13- to 17-week-old)
1104 underwent an intraperitoneal administration of pentylenetetrazole (PTZ, Sigma-Aldrich,
1105 U.S.A.) with 10 mg/kg living weight. PTZ was diluted in sterile Ringer's solution (pH 7.3–7.4)
1106 to a concentration of 5 μg/μL beforehand. All mice received an intraperitoneal injection of PTZ
1107 (40 μL PTZ-solution per 20 g living weight) every ten minutes. All tested animals were
1108 monitored in transparent cages with no additional enrichment. Within every period of ten
1109 minutes, the occurrence of different epileptic events ranked from severity level 0 (no
1110 abnormalities) to most severe score 7 (final tonic-clonic seizure with overstretched limbs and
1111 tail) were detected. For each period of ten minutes, all detected severity scores were added
1112 up and compared between *Sst-Cre/tdTomato* and *Sst-Cre/tdTomato/Dnmt1 LoxP*^{2} mice.
1113 Animals that depicted a final tonic-clonic seizure before the ending of the experiment
1114 (maximum 12 injections and spending 150 min in the setup) were not included in the
1115 calculations after their final epileptic event (score 7). Respective severity levels and
1116 corresponding events are depicted in Figure 6 following Racine's scoring. After PTZ-protocol,
1117 all mice were sacrificed with an overdose of 5 vol% isoflurane followed by cervical dislocation
1118 after reaching surgical tolerance, verified by loss of withdrawal response to toe pinch.
1119

1120 **Statistics and Figure illustration**
1121 Statistical tests were performed using Matlab, Phyton, and GraphPad Prism. Unless otherwise
1122 stated, normally distributed data was tested applying unpaired and two-tailed Student's *t*-test
1123 and an unpaired Welch's *t*-test, nested two-way ANOVA, and two-way ANOVA followed by
1124 Bonferroni correction. For non-normally distributed data we used a Wilcoxon *rank-sum* test.
1125 Respective statistical tests can be found in the main text and individual captions.
1126 Unless otherwise stated, all depicted error bars represent the standard error of the mean
1127 (SEM). Violin plots show the distribution of the numeric data using density curves, with the
1128 respective frequency of data points represented by the width. Straight lines represent the
1129 median and dotted lines the corresponding interquartile range. Single-value plots (XY-graphs)
1130 display all detected data points together with their mean and SEM used to illustrate analyses
1131 including two-way nested ANOVA tests. Data derived from one specimen (embryo, adult
1132 mouse) are illustrated by different shapes of the respective data points and can therefore be
1133 distinguished from values derived from other animals. For boxplots, the central box represents
1134 the interquartile range (IQR), with the median denoted as a horizontal line within the box.
1135 Moreover, the 25th percentile (Q1) and the 75th percentile (Q3) of the data are shown. The
1136 whiskers extend to the data's minimum and maximum values.
1137
1138 **Data Availability**
1139 The sequencing datasets generated and/or analyzed for this study are available in the Gene
1140 Expression Omnibus repository with the following accession numbers: GSE276510,
1141 GSE276512, and GSE276516. The MERESCOPE and sc/snRNA datasets are currently
1142 deposited at GEO and accession numbers will be available upon acceptance. MD simulation
1143 data are uploaded here: https://pubmed.ncbi.nlm.nih.gov/21070939/. Neuropixels recording
1144 data are uploaded here: https://doi.org/10.6084/m9.figshare.28282838.
1145
1146 **Code Availability**
1147 Not applicable.
1148
1149
1150
1151 **Figure Legends**
1152
1153 **Figure 1 – DNMT1 regulates the expression of hub genes of cIN development in**
1154 **migrating E14.5 SST$^+$ interneurons**
1155 **(a-g)** Molecular dynamic simulations of DNMT1 binding to unmethylated DNA (UMDNA)**. (a)**
1156 Inter-unit DNMT1 proteins interacting with the DNMT1/UMDNA/SAH complex unit in the X-ray
1157 structure (PDB ID: 3PTA). Intra-unit DNMT1 regions shown include the autoinhibitory linker
1158 BAH1/BAH2 (white surface), catalytic domain (orange), SAH (red spheres), and CXXC domain
1159 (yellow), which interacts most with UMDNA (blue). The neighboring inter-unit DNMT1 proteins
1160 are illustrated in rose-pink. The inter-unit DNMT1 regions the UMDNA interacts with are mostly
1161 positively charged (**Extended Data Fig. E1b**). **(b-g)** Simulations of DNMT1/UMDNA
1162 interactions in aqueous solution. **(b)** Illustration of the DNMT1/UMDNA complex in solution. **(c)**
1163 The complex at the end of one of our three MD simulations (same coloring scheme as in **(a)**),
1164 with residues at the CpG site interacting with the catalytic domain highlighted by sticks. Only

hydrogen atoms bound to polar groups are shown (as black dash lines). **(d-g)** Number of contacts between UMDNA **(d)**, the 5' **(e)** and 3' regions **(f)** with DNMT1, as well as between the 5' region and the catalytic domain of DNMT1 **(g)** the during last-100-ns simulation (being consistent across replicas (**Extended Fig. E1g, h**).
(h-o) Differential gene expression and methylation analysis of *Sst-Cre/tdTomato* control (ctrl) and *Sst-Cre/tdTomato/Dnmt1 loxP*^{2} (*knockout;* KO) mice based on total RNA and enzymatic methyl-sequencing of FAC-sorted *tdTomato*$^+$ cells isolated from the E14.5 basal telencephalon. For RNA- and methyl-sequencing, we separately processed two samples per genotype, each consisting of cells pooled from multiple embryos (RNA sequencing: Ctrl $n = 23$ embryos; KO $n = 14$ embryos; methyl-sequencing: Ctrl $n = 15$ embryos; KO n = 11 embryos). **(h)** Volcano plot depicting the differentially expressed genes (DEGs) between control and KO samples. Genes annotated as significantly changed (adjusted p-value < 0.05) are colored with red depicting increased expression in KO. **(i)** Heatmap of the 50 genes with the lowest adjusted p-values, color-coded based on relative expression. **(j)** Venn diagram illustrating the overlap between up- or downregulated genes and genes associated with or containing a differentially methylated region (DMR). The intersection of upregulated and differentially methylated genes after knockout was tested for enrichment of the DNMT1 binding motif identified by DNMT1-ChIP-sequencing, shown in k. **(l)** DEGs identified in *Dnmt1* KO samples were compared to DEGs determined in embryonic stem cell-derived murine neurons overexpressing DNMT1. **(m)** Selection of brain development-related gene ontology (GO) terms enriched in genes that were both upregulated and differentially methylated in E14.5 *Sst-Cre/tdTomato/Dnmt1* KO cells. **(k)** DNA motif enriched in DNMT1-interacting chromatin, detected by ChIP-sequencing ($N = 2$ biological replicates). **(n)** Position of differentially methylated regions relative to the transcription start sites of genes related to cIN development. Horizontal bars indicate the region's size, and color-coded is the mean methylation change for the respective region. **(o)** RNA sequencing tracks combined with the methylation profile of the *Arx* gene locus obtained from ctrl and KO samples.

Figure 2: DNMT1 regulates the migration of SST$^+$ interneurons in the developing cortex. **(a)** Schematic illustration of a coronally sectioned E14.5 brain hemisphere, depicting the migration routes of cINs. **(b, c)** Exemplary microphotographs of tdTomato$^+$ interneurons in coronally sectioned (50 μm) hemispheres of *Som-Cre/tdTomato* (control) **(b)** and of *Som-Cre/tdTomato/Dnmt1 loxP*^{2} (KO) embryos **(c)**. tdTomato-positive cells are labeled in red and DAPI in blue. Scale bars: 500 μm. **(d)** Quantification of the proportional distribution of tdTomato$^+$ cells in the basal telencephalon and the cortical wall. Analyses were conducted in E14.5 coronal sections using a nested two-way ANOVA with $n = 12$ sections for control, $n = 8$ sections for KO, and $N = 3$ embryos per genotype. **(e)** Quantification of tdTomato$^+$ cell number within the cortex of control and KO embryos normalized to the area, analyzed in 50 μm coronal cryosections (nested two-way ANOVA with $n = 14$ sections for control, $n = 8$ sections for KO, and $N = 3$ embryos per genotype). **(f)** Schematic illustration of migration trajectories within the E14.5 cortex. **(g, h)** Magnified microphotographs of the cortices of control and KO embryos (E14.5) to illustrate the distribution of tdTomato$^+$ cells within the cortical zones. White asterisks point to cells migrating along the MZ (superficial migratory stream) or deep stream (SVZ/IZ). Yellow arrows indicate tdTomato$^+$ cells located in the CP. Scale bars: 100 μm. **(i)** Quantitative

analysis of the proportional distribution of tdTomato$^+$ cells within the cortical zones normalized to the overall tdTomato$^+$ cell count within the cortex of control and KO embryos at E14.5 analyzed in 50 μm coronal cryosections (nested two-way ANOVA; $n = 14$ sections for control, $n = 8$ sections for KO, and $N = 3$ embryos per genotype). **(j, k)** Temporal z-projections of migration tracks of tdTomato$^+$ cells in organotypic brain slice cultures (350 μm thickness, coronal) from E14.5 *Som-Cre/tdTomato* (control) and *Som-Cre/tdTomato/Dnmt1 loxP^2* (KO) embryos, captured over 20 h by live-cell imaging. Scale bars: 500 μm. **(l-o)** Live-cell imaging quantifications. Quantitative analysis of the increase in fluorescence intensity in the CP reflecting the invasion of tdTomato$^+$ cells (first 12 h, nested two-way ANOVA with $n = 4$ slices for control, $n = 6$ slices for KO embryos, and $N = 3$ embryos per genotype) is shown in **(l)**, the average number of directional changes ($n = 134$ cells across 5 slices for control ($N = 4$ embryos), $n = 74$ cells across 3 slices for KO ($N = 3$ embryos), nested two-way ANOVA) is depicted in **(m)**. The velocity of all cells migrating within the cortex ($n = 377$ cells across 6 slices for control ($N = 5$ embryos), $n = 323$ cells across 5 slices for KO ($N = 3$ embryos)) is shown in **(n),** while the speed of cells within the area between CP and VZ is illustrated in **(o)** for control ($n = 193$ cells across 6 slices, $N = 5$ embryos) and KO ($n = 114$ cells across 3 slices, $N = 3$ embryos); nested two-way ANOVA. **(p, q)** Selected frames extracted from live-cell imaging recordings of organotypic brain slices (350 μm) derived from E14.5 control and KO embryos. Depicted are tdTomato$^+$ cells migrating through the cortex. For each genotype, selected cells (dotted circles) are highlighted. Scale bars: 50 μm.
(r-t) Differential gene expression analysis of FAC-sorted *Sst-Cre/tdTomato* and *Sst-Cre/tdTomato/Dnmt1 loxP^2* cells isolated from the E14.5 cortex. Three samples per genotype were separately processed, consisting of cells pooled from multiple embryos (Ctrl $n = 7$ embryos; KO $n = 8$ embryos). **(r)** Venn diagram illustrating the overlap between upregulated genes in *Sst-Cre/tdTomato/Dnmt1 loxP^2* cells from the basal telencephalon and the cortex (E14.5). **(s)** Heatmap illustrating the log2-fold change for the genes which were upregulated in *Sst-Cre/tdTomato/Dnmt1 loxP^2* cells from the basal telencephalon and the cortex. Moreover, changes in DNA methylation (from the basal telencephalon dataset) are depicted. **(t)** Gene ontology (GO) terms enriched in genes that were upregulated in E14.5 *Sst-Cre/tdTomato/Dnmt1* KO cells from both the basal telencephalon and the cortex.
Error bars represent the standard error of the mean (SEM). $p < 0.05$ *, $p < 0.01$ **, $p < 0.001$ ***; n.s.: not significant. CP: cortical plate, VZ: ventricular zone, SVZ: subventricular zone, MZ: marginal zone, IZ: intermediate zone, l: lateral, m: medial, Ctx: cortex, bTel: basal telencephalon. FC: fold change. Data points with the same symbol depicted in (e) and (l-n) belong to one embryo.

Figure 3: Conditional deletion of *Dnmt1* in SST interneurons affects IPCs and the generation of TBR1$^+$ cells non-cell autonomously. (a, f) Schematic illustrations of a coronally sectioned embryonic brain hemisphere, depicting the lateral and dorsal localization of the two bin selections, used to quantify the density and distribution of EOMES$^+$- and TBR1$^+$-cells in E14.5 and E16.5 brain sections. **(b-e)** TBR1 and EOMES immunostaining in coronally sectioned (50 μm) brains of E14.5 *Sst-Cre/tdTomato* (control) and *Sst-Cre/tdTomato/Dnmt1 loxP^2* (KO) embryos. **(b** and **d)** Exemplary microphotographs of (**b**) TBR1 immunostaining (green) and **(d)** EOMES immunostaining (green); scale bars: 50 μm (DAPI is shown in blue).

1254 **(c** and **e)** Quantitative analysis of the TBR1$^+$ postmitotic neuron numbers **(c)** and EOMES$^+$
1255 intermediate progenitor cell (IPC) numbers **(e)** per bin in E14.5 cortices of control and KO
1256 embryos, analyzed in 50 μm coronal cryosections (two-way ANOVA with subsequent
1257 Bonferroni correction, n = 13 control and n = 9 KO sections from N = 3 embryos for both
1258 genotypes). **(g)** TBR1 immunostaining (green) in coronally sectioned (50 μm) brains of E16.5
1259 control and KO embryos, scale bars: 50 μm. DAPI is depicted in blue. **(h)** Quantitative analysis
1260 of the TBR1$^+$ postmitotic neuron numbers per bin in the E16.5 cortex of control and KO
1261 embryos, analyzed in 50 μm coronal cryosections (two-way ANOVA with subsequent
1262 Bonferroni correction, n = 8 for control and KO from N = 3 embryos for both genotypes). **(i)**
1263 EOMES immunostaining (green) in coronally sectioned (50 μm) brains of E16.5 control and
1264 KO embryos, scale bars: 50 μm. DAPI is depicted in blue. **(j)** Quantitative analysis of the
1265 EOMES$^+$ postmitotic neuron numbers per bin in the E16.5 cortex of control and KO embryos,
1266 analyzed in 50 μm coronal cryosections (two-way ANOVA with subsequent Bonferroni
1267 correction, n = 15 control and n= 13 KO sections from N = 3 embryos for both genotypes). **(k)**
1268 Schematic illustration of a coronally sectioned E18.5 embryonic brain hemisphere, depicting
1269 the lateral and dorsal localizations used to quantify the density and distribution of EOMES$^+$-
1270 and TBR1$^+$-cells. **(l** and **n)** Exemplary microphotographs of (**l**) EOMES immunostaining (green)
1271 and **(n)** TBR1 immunostaining (green) in coronal sections of E18.5 control and KO brains;
1272 scale bars: 50 μm (DAPI is shown in blue). **(m** and **o)** Quantitative analyses of the total
1273 numbers and densities of EOMES$^+$IPCs **(m)** and TBR1$^+$postmitotic neurons **(o)** in the E18.5
1274 cortex of control and KO embryos, analyzed in 50 μm coronal cryosections. Additionally, the
1275 area of the IZ-VZ and the CP was analyzed in **(m)** and **(o)**, respectively (nested two-way
1276 ANOVA with n = 11 sections for both genotypes from N = 4 embryos, respectively). **(p)**
1277 Schematic illustration of the cortex of a coronally sectioned embryonic brain (E18.5), depicting
1278 the parameters analyzed for the quantification shown in (**q**). Three regions (lateral (1),
1279 dorsolateral (2), and dorsal (3)) were averaged to obtain the mean thickness respectively for
1280 each layer (nested two-way ANOVA with n = 12 control and n = 9 KO sections. N = 4 brains
1281 for both genotypes).
1282 $p < 0.05$ *, $p < 0.01$ **, $p < 0.001$ ***. MZ: marginal zone, CP: cortical plate, IZ-VZ: intermediate
1283 zone-ventricular zone, ctrl.: control, n.s.: not significant. Data points depicted in (m), (o), and
1284 (p) with the same symbol arise from the same embryo.
1285
1286 **Figure 4: Single-cell resolution approaches reveal non-cell-autonomous effects of SST+**
1287 **interneurons on cortical progenitors a, b)** Single-cell RNA sequencing (scRNA-seq) of
1288 dorsal telencephalons from E14.5 C57BL/6J mice identifies significant ligand-receptor
1289 interactions mediating communication from SST+ cINs to **(a)** different apical cortical progenitor
1290 populations (APs) and **(b)** to intermediate progenitors (IPCs), filtered by differentially
1291 expressed genes (DEG). Communication probability is represented by dot color, and the
1292 corresponding p-value by dot size, with p-values being computed using a one-sided
1293 permutation test. **(c-f)** Pair cell assay performed with cortical neurons isolated from E14.5
1294 C57BL6/J embryos, plated at clonal density. Cell clones were either treated with control (ctrl)-
1295 or recombinant efnB2-Fc for 24 h, before immunocytochemical staining for nestin (NES,
1296 magenta), β-III-tubulin (TUBB3, green), EOMES (yellow) and DAPI (blue). Scale bars: 5 μm.
1297 **(d** and **f)** Quantification of the proportion of nestin/nestin (2xN), β-III-tubulin/β-III-tubulin (2xT),
1298 nestin/β-III-tubulin (N-T), EOMES-EOMES (2xE), and nestin-EOMES (N-E) positive cell pairs

normalized to the overall number of these pairs. Unpaired Welch's *t*-test with control-Fc: n = 90 cell pairs, efnB2-Fc: n = 91 cell pairs, from N = 4 experiments in **d**; and control-Fc: n = 90 cell pairs, efnB2-Fc: n = 94 cell pairs, from N = 4 experiments in **f**. **(g-l)** Single nuclear RNA (snRNA) sequencing of cortical cells prepared from E16.5 *Sst-Cre/tdTomato* and *Sst-Cre/tdTomato/Dnmt1 loxP*^{2} embryos (n = 2 brains from N =2 mice per genotype). **(g)** UMAP illustrating cell clusters determined by snRNA sequencing across all samples. **(h)** Dot plot depicting marker gene expression in the different cell clusters. **(i)** Bar plot showing the proportional distribution of the cell numbers determined for all postmitotic excitatory cortical neurons. **(j)** Venn diagram illustrating the overlay of the upregulated genes in E14.5 cortical FAC-sorted *Sst-Cre/tdTomato/Dnmt1 loxP*^{2} cells (bulk RNA sequencing) compared to *Sst-Cre/tdTomato* samples, with the upregulated genes found in E16.5 cortical *Sst*$^+$*/Gad*$^+$ cells form *Sst-Cre/tdTomato/Dnmt1 loxP*^{2} compared to *Sst-Cre/tdTomato* samples (snRNA sequencing). **(j, k, l)** Interaction maps extracted with CellChat from the snRNA sequencing dataset of E16.5 cortices from *Sst-Cre/tdTomato/Dnmt1 loxP*^{2} and *Sst-Cre/tdTomato* embryos, depicting number of interactions **(k)** and interaction strength **(l)**. **(m-p)** Multiplexed spatial transcriptomics analysis of E16.5 *Sst-Cre/tdTomato/Dnmt1 loxP*^{2} and *Sst-Cre/tdTomato* brain sections using MERFISH. **(m)** UMAP visualization of distinct cell clusters identified based on gene expression profiles. **(n)** Representative tissue sections with spatially resolved cell clusters mapped onto anatomical regions, scale bar 1000 μm. **(o)** Magnified sections from the cortex Scale bar = 100 μm. **(p)** Cluster annotation for (m-o). $p < 0.05$ *, $p < 0.01$ **, $p < 0.001$ ***. n.s.: not significant.

Figure 5: Adult *Dnmt1*-deficient mice show aberrant cortical architecture and functionality. (a-d) *Dnmt1* KO mice display changes in cortical layer thickness alongside alterations in *Sst-Cre/tdTomato* cell density. **(a, b)** Exemplary microphotographs of immunostainings of CUX1 and tdTomato combined with DAPI taken from S1 (sagittal slices of Bregma 1.32 and 1.44, six-month-old male mice). The CUX1$^+$ supragranular layers II-IV can be distinguished from infragranular layers V and VI. Scale bars: 100 μm. **(c, d)** Quantification of the tdTomato$^+$ cell density normalized to the given area of the respective layers (**c**), the cortical thickness, and the proportional thickness of the deep and upper layers (**d**). Nested two-way ANOVA with n = 24 slices for control and n = 23 for KO from N = 3 brains for both genotypes. $p < 0.05$ *, $p < 0.01$ **, $p < 0.001$ ***, n.s.: not significant. Data points depicted in (c and d) with the same symbol arise from the same mouse.
(e) Left: Neuropixels recordings in S1 of head-fixed control and *Dnmt1* KO mice, running on a wheel. Right: Example brain slice from S1, showing red dye fluorescence from the probe. The scheme visualizes the probe position. **(f)** Average current source density (CSD) across the whole cortical depth in S1, following a 20 ms tactile stimulus (white line) to the distal whisker pad. Blue colors indicate excitatory and yellow colors inhibitory currents. The earliest responses in control mice (left) occurred in the granular layer at ~400 μm cortical depth and then spread to layer II/III (100-300 μm) and layer V (500-900 μm). In contrast, responses were much weaker and less spatially defined in KO mice. Matching the anatomical results, response differences to controls were largest in the supragranular layers. **(g)** Quantification of CSD response peaks across sessions for each group. Supragranular responses above 400 μm were significantly lower and delayed in *Dnmt1* KO versus control mice (peak amplitude$_{control}$ = -4.74 ± 1.22 μA/mm^3, peak amplitude$_{KO}$ = -1.41 ± 0.18 μA/mm^3, p = 0. 0037; peak time$_{control}$ =

27.20 ± 0.84 ms, peak time$_{KO}$ = 31.80 ± 1.03 ms, p = 0.0041; n = 8 sessions from 2 mice per group). **(h)** CSD traces in S1, averaged over tactile responses in either supragranular (top) or infragranular layers (bottom). Clearly visible are reduced and delayed responses in supragranular layers for *Dnmt1* KO mice (orange). Same data as in panels (f) and (g). **(i)** Peristimulus time histogram (PSTH) for the spiking response of S1 neurons in supra- or infragranular layers to tactile stimulation in KO (orange) and control mice (gray). **(j)** Spectral power density (PSD) of LFP recordings across all layers in either S1 (left) or primary visual cortex (V1, right). In both cortical areas, PSDs fall off with frequency but remain significantly higher in the high-frequency gamma range from 30-90 Hz for control versus KO mice (S1: gamma power$_{control}$ = -23.69 ± 21.32 dBmV, gamma power$_{KO}$ = -61.95 ± 3.19 dBmV, p = 0.0378; V1: gamma power$_{control}$ = -25.65 ± 8.65 dBmV, gamma power$_{KO}$ = -68.27 ± 4.38 dBmV, p = 0.0037; n = 8 sessions from 2 mice per group). **(k)** Stimulus-induced change in PSD in V1, computed as the percent difference relative to baseline. Full-field visual stimulation induced a strong increase in V1 gamma power (> 30 Hz), especially around 70 Hz, in control mice. In contrast, stimulus-induced modulation was much weaker in KO mice (relative gamma$_{control}$ = 104.25 ± 24.42%, relative gamma$_{KO}$ = 28.71 ± 6.31%, p = 0.0018; n = 8 sessions from 2 mice per group). **(l)** Stimulus-induced change in PSD gamma power across cortical depth. Changes in control mice were largest between 0.3- and 0.7-mm but largely absent in KO mice. Significance for panels g, j, and k was based on a Wilcoxon *rank-sum* test, values are mean ± SEM. Shading in panels h, i, and k show the SEM.

Figure 6: Adult *Dnmt1*-deficient mice show behavioral abnormalities.

(a) Example images of a head-fixed *Dnmt1* KO mouse before and during an epileptiform event with dilated pupil and postural changes (white circles). **(b)** Example trace and spectrogram from cortical LFP recording during the event show a strong increase in theta oscillations for ~30 seconds. Times of video images 1 and 2 (white numbers in (a)) are shown as gray lines in the top trace. **(c)** Quantification of LFP deflections across depth for a 2-second time window during the event.

(d-f) Pentylenetetrazol (PTZ)-injections every 10 min in three months old *Sst-Cre/tdTomato* (control) and *Sst-Cre/tdTomato/Dnmt1 loxP*^{2} males (*Dnmt1* KO) point to defects in cortical inhibition in KO mice. **(d)** Schematic illustrations defining PTZ-induced seizures using Racine's scoring: 1: immobilization by sudden arrest and lying flat on the ground for several seconds up to minutes. 2: facial twerking, intensive mouth movement, and/or teeth grinding without convulsions. 3: frequent head nodding and/or partial myoclonic events (mostly unilateral limb- or tail clonus). 4: continuous whole-body myoclonus indicated by a stretched back, as well as extensive and dynamic stiffening of the tail with overhead pointing towards the rostrum. 5: clonic seizure characterized by unilateral forelimb clonus and bending over until reaching a sitting/standing position. 6: clonic-tonic seizure with falling on one side, wild rushing, and jumping. 7: Generalized tonic-clonic seizure is indicated by wild rushing, jumping, and tonic extension cumulating in overstretched limbs and tail. This epileptiform event results in respiratory depression and/or death (end of the experiment). (**e**) Footages captured from video monitoring of PTZ-induced convulsions for respective Racine's scores, that are depicted in (d). (**f**) Heat maps and quantification of Racine's scale events associated with the given number of PTZ-injections or passed time. Within every column (illustrating the number of applied injections (left) or minutes after the first injection of PTZ (right)), all detected epileptiform events

were correlated to their respective severity score (0-7), added up, and averaged for each genotype (rows). *Dnmt1*-KO mice show significantly higher Racine's scale points (=severity levels) indicated by red colors. Wilcoxon *rank-sum* test, $p < 0.05$ *, $p < 0.01$ **, $p < 0.001$ ***. $N = 10$ animals per genotype. **(g-j)** Nest building test reveals a significant deterioration in using given material and forming proper nests in adult *Sst-Cre/tdTomato/Dnmt1* loxP[2] (KO) animals compared to *Sst-Cre/tdTomato* (control) mice. With the help of the scoring index depicted in (**g**) and formerly described[94], all mice were ranked based on nest quality and the amount of used material (**h-j**). Representative photographs are shown in (**h**) for control and KO mice. Tests were performed overnight and twice within one week. Respective values were averaged for both trials (**i, j**). Unpaired, two-tailed Student's *t*-test and additional unpaired Welch's *t*-test. $N = 16$ male adult mice for both genotypes.

References

1. Vanderhaeghen, P. & Polleux, F. Developmental mechanisms underlying the evolution of human cortical circuits. *Nat Rev Neurosci* **24**, 213–232 (2023).
2. Delaunay, D., Kawaguchi, A., Dehay, C. & Matsuzaki, F. Division modes and physical asymmetry in cerebral cortex progenitors. *Current Opinion in Neurobiology* **42**, 75–83 (2017).
3. Lin, Y. *et al.* Behavior and lineage progression of neural progenitors in the mammalian cortex. *Current Opinion in Neurobiology* **66**, 144–157 (2021).
4. Harris, K. D. & Shepherd, G. M. G. The neocortical circuit: themes and variations. *Nat Neurosci* **18**, 170–181 (2015).
5. Gerstmann, K. *et al.* Thalamic afferents influence cortical progenitors via ephrin A5-EphA4 interactions. *Development* **142**, 140–150 (2015).
6. Gerstmann, K. *et al.* A balance of noncanonical Semaphorin signaling from the cerebrospinal fluid regulates apical cell dynamics during corticogenesis. *Sci. Adv.* **8**, eabo4552 (2022).
7. Gerstmann, K. & Zimmer, G. The role of the Eph/ephrin family during cortical development and cerebral malformations. (2018).
8. Reillo, I. *et al.* A Complex Code of Extrinsic Influences on Cortical Progenitor Cells of Higher Mammals. *Cerebral Cortex* **27**, 4586–4606 (2017).
9. Villalba, A., Götz, M. & Borrell, V. The regulation of cortical neurogenesis. in *Current Topics in Developmental Biology* vol. 142 1–66 (Elsevier, 2021).
10. Silva, C. G. *et al.* Cell-Intrinsic Control of Interneuron Migration Drives Cortical Morphogenesis. *Cell* **172**, 1063-1078.e19 (2018).
11. Kepecs, A. & Fishell, G. Interneuron cell types are fit to function. *Nature* **505**, 318–326 (2014).
12. Kessaris, N. & Denaxa, M. Cortical interneuron specification and diversification in the era of big data. *Current Opinion in Neurobiology* **80**, 102703 (2023).
13. Lim, L., Mi, D., Llorca, A. & Marín, O. Development and Functional Diversification of Cortical Interneurons. *Neuron* **100**, 294–313 (2018).
14. Wonders, C. P. & Anderson, S. A. The origin and specification of cortical interneurons. *Nat Rev Neurosci* **7**, 687–696 (2006).
15. Reichard, J. & Zimmer-Bensch, G. The Epigenome in Neurodevelopmental Disorders. *Front. Neurosci.* **15**, 776809 (2021).
16. Fogarty, M. *et al.* Spatial Genetic Patterning of the Embryonic Neuroepithelium Generates GABAergic Interneuron Diversity in the Adult Cortex. *J. Neurosci.* **27**, 10935–10946 (2007).

1441 17. Butt, S. J. B. *et al.* The Temporal and Spatial Origins of Cortical Interneurons Predict
1442 Their Physiological Subtype. *Neuron* **48**, 591–604 (2005).
1443 18. Niquille, M. *et al.* Neurogliaform cortical interneurons derive from cells in the preoptic
1444 area. *eLife* **7**, e32017 (2018).
1445 19. Gelman, D. M. *et al.* The Embryonic Preoptic Area Is a Novel Source of Cortical
1446 GABAergic Interneurons. *J. Neurosci.* **29**, 9380–9389 (2009).
1447 20. Zimmer, G. *et al.* Bidirectional ephrinB3/EphA4 signaling mediates the segregation of
1448 MGE and POA derived interneurons in the deep and superficial migratory stream. *J*
1449 *Neuroscience* **50**, (2011).
1450 21. Zimmer, G. *et al.* Chondroitin Sulfate Acts in Concert with Semaphorin 3A to Guide
1451 Tangential Migration of Cortical Interneurons in the Ventral Telencephalon. *Cerebral Cortex*
1452 **20**, 2411–2422 (2010).
1453 22. Zimmer, G. *et al.* Ephrin-A5 acts as a repulsive cue for migrating cortical
1454 interneurons. *Eur J of Neuroscience* **28**, 62–73 (2008).
1455 23. Zimmer-Bensch, G. Diverse facets of cortical interneuron migration regulation -
1456 Implications of neuronal activity and epigenetics. *Brain research* **1700**, 160–169 (2018).
1457 24. Lim, Y. *et al.* ARX regulates cortical interneuron differentiation and migration. Preprint
1458 at https://doi.org/10.1101/2024.01.31.578282 (2024).
1459 25. Wang, Y. *et al.* CXCR4 and CXCR7 Have Distinct Functions in Regulating
1460 Interneuron Migration. *Neuron* **69**, 61–76 (2011).
1461 26. Bartolini, G. *et al.* Neuregulin 3 Mediates Cortical Plate Invasion and Laminar
1462 Allocation of GABAergic Interneurons. *Cell Reports* **18**, 1157–1170 (2017).
1463 27. Yildiz, C. B. & Zimmer-Bensch, G. Role of DNMTs in the Brain. *Adv Exp Med Biol*
1464 **1389**, 363–394 (2022).
1465 28. Pensold, D. *et al.* The DNA Methyltransferase 1 (DNMT1) Controls the Shape and
1466 Dynamics of Migrating POA-Derived Interneurons Fated for the Murine Cerebral Cortex.
1467 *Cereb Cortex* **27**, 5696–5714 (2017).
1468 29. Urban-Ciecko, J. & Barth, A. L. Somatostatin-expressing neurons in cortical networks.
1469 *Nat Rev Neurosci* **17**, 401–409 (2016).
1470 30. Liodis, P. *et al. Lhx6* Activity Is Required for the Normal Migration and Specification of
1471 Cortical Interneuron Subtypes. *J. Neurosci.* **27**, 3078–3089 (2007).
1472 31. Lim, L. *et al.* Optimization of interneuron function by direct coupling of cell migration
1473 and axonal targeting. *Nat Neurosci* **21**, 920–931 (2018).
1474 32. Kikuchi, A. *et al.* Structural basis for activation of DNMT1. *Nat Commun* **13**, 7130
1475 (2022).
1476 33. Song, J., Rechkoblit, O., Bestor, T. H. & Patel, D. J. Structure of DNMT1-DNA
1477 Complex Reveals a Role for Autoinhibition in Maintenance DNA Methylation. *Science* **331**,
1478 1036–1040 (2011).
1479 34. Pradhan, M. *et al.* CXXC Domain of Human DNMT1 Is Essential for Enzymatic
1480 Activity. *Biochemistry* **47**, 10000–10009 (2008).
1481 35. Hutnick, L. K. *et al.* DNA hypomethylation restricted to the murine forebrain induces
1482 cortical degeneration and impairs postnatal neuronal maturation. *Human molecular genetics*
1483 **18**, 2875–88 (2009).
1484 36. Pensold, D. *et al.* DNA Methylation-Mediated Modulation of Endocytosis as Potential
1485 Mechanism for Synaptic Function Regulation in Murine Inhibitory Cortical Interneurons.
1486 *Cereb Cortex* **30**, 3921–3937 (2020).
1487 37. Kadriu, B., Guidotti, A., Chen, Y. & Grayson, D. R. DNA methyltransferases1
1488 (DNMT1) and 3a (DNMT3a) colocalize with GAD67-positive neurons in the GAD67-GFP
1489 mouse brain. *The Journal of comparative neurology* **520**, 1951–64 (2012).
1490 38. Elbert, A. *et al.* CTCF Governs the Identity and Migration of MGE-Derived Cortical
1491 Interneurons. *J. Neurosci.* **39**, 177–192 (2019).
1492 39. Munguba, H. *et al.* Transcriptional maintenance of cortical somatostatin interneuron
1493 subtype identity during migration. *Neuron* **111**, 3590-3603.e5 (2023).
1494 40. Taniguchi, H. *et al.* A Resource of Cre Driver Lines for Genetic Targeting of
1495 GABAergic Neurons in Cerebral Cortex. *Neuron* **71**, 995–1013 (2011).
1496 41. Hu, J. S., Vogt, D., Sandberg, M. & Rubenstein, J. L. Cortical interneuron

development: a tale of time and space. *Development* **144**, 3867–3878 (2017).
42. Gustafsson, J. R. *et al.* DNMT1 regulates expression of MHC class I in post-mitotic neurons. *Mol Brain* **11**, 36 (2018).
43. Feng, J. *et al.* Dnmt1 and Dnmt3a maintain DNA methylation and regulate synaptic function in adult forebrain neurons. *Nat Neurosci* **13**, 423–430 (2010).
44. Singh, M., Saxena, S. & Mohan, K. N. DNMT1 downregulation as well as its overexpression distinctly affect mostly overlapping genes implicated in schizophrenia, autism spectrum, epilepsy, and bipolar disorders. *Front. Mol. Neurosci.* **16**, 1275697 (2023).
45. Nan, X. *et al.* Transcriptional repression by the methyl-CpG-binding protein MeCP2 involves a histone deacetylase complex. *Nature* **393**, 386–389 (1998).
46. Gabel, H. W. *et al.* Disruption of DNA-methylation-dependent long gene repression in Rett syndrome. *Nature* **522**, 89–93 (2015).
47. Mayer, C. *et al.* Developmental diversification of cortical inhibitory interneurons. *Nature* **555**, 457–462 (2018).
48. Gruner, H. N., Kim, M. & Mastick, G. S. Robo1 and 2 Repellent Receptors Cooperate to Guide Facial Neuron Cell Migration and Axon Projections in the Embryonic Mouse Hindbrain. *Neuroscience* **402**, 116–129 (2019).
49. Talebian, A. *et al.* Autonomous and non-autonomous roles for ephrin-B in interneuron migration. *Developmental Biology* **431**, 179–193 (2017).
50. Marín, O., Yaron, A., Bagri, A., Tessier-Lavigne, M. & Rubenstein, J. L. Sorting of striatal and cortical interneurons regulated by semaphorin-neuropilin interactions. *Science* **293**, 872–875 (2001).
51. Boyes, J. & Bird, A. DNA methylation inhibits transcription indirectly via a methyl-CpG binding protein. *Cell* **64**, 1123–1134 (1991).
52. Sharma, A., Klein, S. S., Barboza, L., Lohdi, N. & Toth, M. Principles Governing DNA Methylation during Neuronal Lineage and Subtype Specification. *J Neurosci* **36**, 1711–1722 (2016).
53. Lister, R. *et al.* Global Epigenomic Reconfiguration During Mammalian Brain Development. *Science* **341**, 1237905 (2013).
54. van den Berghe, V. *et al.* Directed Migration of Cortical Interneurons Depends on the Cell-Autonomous Action of Sip1. *Neuron* **77**, 70–82 (2013).
55. McKinsey, G. L. *et al.* Dlx1&2-Dependent Expression of Zfhx1b (Sip1, Zeb2) Regulates the Fate Switch between Cortical and Striatal Interneurons. *Neuron* **77**, 83–98 (2013).
56. Pai, E. L.-L. *et al.* Maf and Mafb control mouse pallial interneuron fate and maturation through neuropsychiatric disease gene regulation. *eLife* **9**, e54903 (2020).
57. Wang, Y. *et al.* Dlx5 and Dlx6 regulate the development of parvalbumin-expressing cortical interneurons. *J Neurosci* **30**, 5334–5345 (2010).
58. Rudolph, J. *et al.* A dual role of EphB1/ephrin-B3 reverse signaling on migrating striatal and cortical neurons originating in the preoptic area: should I stay or go away? *Front. Cell. Neurosci.* **8**, (2014).
59. Sessa, A. *et al.* Tbr2-positive intermediate (basal) neuronal progenitors safeguard cerebral cortex expansion by controlling amplification of pallial glutamatergic neurons and attraction of subpallial GABAergic interneurons. *Genes Dev.* **24**, 1816–1826 (2010).
60. Kischel, A., Audouard, C., Fawal, M.-A. & Davy, A. Ephrin-B2 paces neuronal production in the developing neocortex. *BMC Dev Biol* **20**, 12 (2020).
61. Jin, S. *et al.* Inference and analysis of cell-cell communication using CellChat. *Nat Commun* **12**, 1088 (2021).
62. Hevner, R. F. *et al.* Tbr1 Regulates Differentiation of the Preplate and Layer 6. *Neuron* **29**, 353–366 (2001).
63. Bulfone, A. *et al.* T-Brain-1: A homolog of Brachyury whose expression defines molecularly distinct domains within the cerebral cortex. *Neuron* **15**, 63–78 (1995).
64. Vasistha, N. A. *et al.* Cortical and Clonal Contribution of Tbr2 Expressing Progenitors in the Developing Mouse Brain. *Cereb. Cortex* **25**, 3290–3302 (2015).
65. Kowalczyk, T. *et al.* Intermediate neuronal progenitors (basal progenitors) produce pyramidal-projection neurons for all layers of cerebral cortex. *Cereb Cortex* **19**, 2439–2450

(2009).
66. Mihalas, A. B. *et al.* Intermediate Progenitor Cohorts Differentially Generate Cortical Layers and Require Tbr2 for Timely Acquisition of Neuronal Subtype Identity. *Cell Reports* **16**, 92–105 (2016).
67. Harrison-Uy, S. J. & Pleasure, S. J. Wnt Signaling and Forebrain Development. *Cold Spring Harbor Perspectives in Biology* **4**, a008094–a008094 (2012).
68. Nian, F.-S. & Hou, P.-S. Evolving Roles of Notch Signaling in Cortical Development. *Front. Neurosci.* **16**, 844410 (2022).
69. Smith, A., Robinson, V., Patel, K. & Wilkinson, D. G. The EphA4 and EphB1 receptor tyrosine kinases and ephrin-B2 ligand regulate targeted migration of branchial neural crest cells. *Current Biology* **7**, 561–570 (1997).
70. Riedemann, T. Diversity and Function of Somatostatin-Expressing Interneurons in the Cerebral Cortex. *IJMS* **20**, 2952 (2019).
71. Nassar, M. *et al.* Diversity and overlap of parvalbumin and somatostatin expressing interneurons in mouse presubiculum. *Front. Neural Circuits* **9**, (2015).
72. Ward, C. *et al.* Developmental Disruption of Mef2c in Medial Ganglionic Eminence–Derived Cortical Inhibitory Interneurons Impairs Cellular and Circuit Function. *Biological Psychiatry* S000632232401360X (2024) doi:10.1016/j.biopsych.2024.05.021.
73. Allaway, K. C. *et al.* Genetic and epigenetic coordination of cortical interneuron development. *Nature* **597**, 693–697 (2021).
74. Musall, S., Kaufman, M. T., Juavinett, A. L., Gluf, S. & Churchland, A. K. Single-trial neural dynamics are dominated by richly varied movements. *Nat Neurosci* **22**, 1677–1686 (2019).
75. Pettersen, K. H., Devor, A., Ulbert, I., Dale, A. M. & Einevoll, G. T. Current-source density estimation based on inversion of electrostatic forward solution: Effects of finite extent of neuronal activity and conductivity discontinuities. *Journal of Neuroscience Methods* **154**, 116–133 (2006).
76. Petersen, C. C. H. The Functional Organization of the Barrel Cortex. *Neuron* **56**, 339–355 (2007).
77. Fries, P., Reynolds, J. H., Rorie, A. E. & Desimone, R. Modulation of Oscillatory Neuronal Synchronization by Selective Visual Attention. *Science* **291**, 1560–1563 (2001).
78. Veit, J., Hakim, R., Jadi, M. P., Sejnowski, T. J. & Adesnik, H. Cortical gamma band synchronization through somatostatin interneurons. *Nat Neurosci* **20**, 951–959 (2017).
79. Ahnaou, A., Huysmans, H., Van De Casteele, T. & Drinkenburg, W. H. I. M. Cortical high gamma network oscillations and connectivity: a translational index for antipsychotics to normalize aberrant neurophysiological activity. *Transl Psychiatry* **7**, 1285 (2017).
80. Yamamoto, J., Suh, J., Takeuchi, D. & Tonegawa, S. Successful Execution of Working Memory Linked to Synchronized High-Frequency Gamma Oscillations. *Cell* **157**, 845–857 (2014).
81. Mandhane, S. N., Aavula, K. & Rajamannar, T. Timed pentylenetetrazol infusion test: A comparative analysis with s.c.PTZ and MES models of anticonvulsant screening in mice. *Seizure* **16**, 636–644 (2007).
82. Racine, R. J. Modification of seizure activity by electrical stimulation: II. Motor seizure. *Electroencephalography and Clinical Neurophysiology* **32**, 281–294 (1972).
83. Liguz-Lecznar, M., Dobrzanski, G. & Kossut, M. Somatostatin and Somatostatin-Containing Interneurons—From Plasticity to Pathology. *Biomolecules* **12**, 312 (2022).
84. Perry, G., Brindley, L. M., Muthukumaraswamy, S. D., Singh, K. D. & Hamandi, K. Evidence for increased visual gamma responses in photosensitive epilepsy. *Epilepsy Research* **108**, 1076–1086 (2014).
85. Kas, M. J. H., Fernandes, C., Schalkwyk, L. C. & Collier, D. A. Genetics of behavioural domains across the neuropsychiatric spectrum; of mice and men. *Mol Psychiatry* **12**, 324–330 (2007).
86. Gaitatzis, A. The Comorbidity of Epilepsy: Epidemiology, Mechanisms and Consequences. in *Atlas of Epilepsies* (ed. Panayiotopoulos, C. P.) 1325–1329 (Springer London, London, 2010). doi:10.1007/978-1-84882-128-6_195.
87. Kraeuter, A.-K., Guest, P. C. & Sarnyai, Z. The Nest Building Test in Mice for

Assessment of General Well-Being. in *Pre-Clinical Models* (ed. Guest, P. C.) vol. 1916 87–91 (Springer New York, New York, NY, 2019).
88. Butler, J. S., Lee, J.-H. & Skalnik, D. G. CFP1 Interacts with DNMT1 Independently of Association with the Setd1 Histone H3K4 Methyltransferase Complexes. *DNA and Cell Biology* **27**, 533–543 (2008).
89. Arand, J. *et al.* In Vivo Control of CpG and Non-CpG DNA Methylation by DNA Methyltransferases. *PLoS Genet* **8**, e1002750 (2012).
90. Fatemi, M., Hermann, A., Gowher, H. & Jeltsch, A. Dnmt3a and Dnmt1 functionally cooperate during *de novo* methylation of DNA. *European Journal of Biochemistry* **269**, 4981–4984 (2002).
91. Jair, K.-W. *et al. De novo* CpG Island Methylation in Human Cancer Cells. *Cancer Research* **66**, 682–692 (2006).
92. Symmank, J. *et al.* DNMT1 modulates interneuron morphology by regulating Pak6 expression through crosstalk with histone modifications. *Epigenetics* **13**, 536–556 (2018).
93. Kremer, L. P. M. *et al.* DNA methylation controls stemness of astrocytes in health and ischaemia. *Nature* **634**, 415–423 (2024).
94. Chenn, A. & Walsh, C. A. Regulation of Cerebral Cortical Size by Control of Cell Cycle Exit in Neural Precursors. *Science* **297**, 365–369 (2002).
95. Deacon, R. M. Assessing nest building in mice. *Nat Protoc* **1**, 1117–1119 (2006).
96. Case, D. A. *et al.* The Amber biomolecular simulation programs. *J Comput Chem* **26**, 1668–1688 (2005).
97. Darden, T., York, D. & Pedersen, L. Particle mesh Ewald: An $N \cdot \log(N)$ method for Ewald sums in large systems. *The Journal of Chemical Physics* **98**, 10089–10092 (1993).
98. Allen, M. P. & Tildesley, D. J. *Computer Simulation of Liquids*. (Oxford University PressOxford, 2017). doi:10.1093/oso/9780198803195.001.0001.
99. Berendsen, H. J. C., Postma, J. P. M., Van Gunsteren, W. F., DiNola, A. & Haak, J. R. Molecular dynamics with coupling to an external bath. *The Journal of Chemical Physics* **81**, 3684–3690 (1984).
100. Roe, D. R. & Cheatham, T. E. PTRAJ and CPPTRAJ: Software for Processing and Analysis of Molecular Dynamics Trajectory Data. *J. Chem. Theory Comput.* **9**, 3084–3095 (2013).
101. Symmank, J., Gölling, V., Gerstmann, K. & Zimmer, G. The Transcription Factor LHX1 Regulates the Survival and Directed Migration of POA-derived Cortical Interneurons. *Cereb Cortex* **29**, 1644–1658 (2019).
102. Hahn, A. *et al.* DNA Methyltransferase 1 (DNMT1) Function Is Implicated in the Age-Related Loss of Cortical Interneurons. *Frontiers in cell and developmental biology* **8**, 639 (2020).
103. Schindelin, J. *et al.* Fiji: an open-source platform for biological-image analysis. *Nat Methods* **9**, 676–682 (2012).
104. Saxena, S., Maroju, P. A., Choudhury, S., Anne, A. & Mohan, K. N. Analysis of transcript levels of a few schizophrenia candidate genes in neurons from a transgenic mouse embryonic stem cell model overexpressing DNMT1. *Gene* **757**, 144934 (2020).
105. Ewels, P. A. *et al.* The nf-core framework for community-curated bioinformatics pipelines. *Nat Biotechnol* **38**, 276–278 (2020).
106. Di Tommaso, P. *et al.* Nextflow enables reproducible computational workflows. *Nat Biotechnol* **35**, 316–319 (2017).
107. Krueger, F., James, F., Ewels, P., Afyounian, E. & Schuster-Boeckler, B. FelixKrueger/TrimGalore: v0.6.7 - DOI via Zenodo. Zenodo https://doi.org/10.5281/ZENODO.5127899 (2021).
108. Dobin, A. *et al.* STAR: ultrafast universal RNA-seq aligner. *Bioinformatics* **29**, 15–21 (2013).
109. Patro, R., Duggal, G., Love, M. I., Irizarry, R. A. & Kingsford, C. Salmon provides fast and bias-aware quantification of transcript expression. *Nat Methods* **14**, 417–419 (2017).
110. Love, M. I., Huber, W. & Anders, S. Moderated estimation of fold change and dispersion for RNA-seq data with DESeq2. *Genome Biol* **15**, 550 (2014).
111. Bolger, A. M., Lohse, M. & Usadel, B. Trimmomatic: a flexible trimmer for Illumina

sequence data. *Bioinformatics* **30**, 2114–2120 (2014).
112. Krueger, F. & Andrews, S. R. Bismark: a flexible aligner and methylation caller for Bisulfite-Seq applications. *Bioinformatics* **27**, 1571–1572 (2011).
113. Feng, H., Conneely, K. N. & Wu, H. A Bayesian hierarchical model to detect differentially methylated loci from single nucleotide resolution sequencing data. *Nucleic Acids Research* **42**, e69–e69 (2014).
114. Hinrichs, A. S. The UCSC Genome Browser Database: update 2006. *Nucleic Acids Research* **34**, D590–D598 (2006).
115. Robinson, J. T. *et al.* Integrative genomics viewer. *Nat Biotechnol* **29**, 24–26 (2011).
116. Harrison, P. W. *et al.* Ensembl 2024. *Nucleic Acids Res* **52**, D891–D899 (2024).
117. Buske, F. A., Bodén, M., Bauer, D. C. & Bailey, T. L. Assigning roles to DNA regulatory motifs using comparative genomics. *Bioinformatics* **26**, 860–866 (2010).
118. Ge, S. X., Jung, D. & Yao, R. ShinyGO: a graphical gene-set enrichment tool for animals and plants. *Bioinformatics* **36**, 2628–2629 (2020).
119. Hao, Y. *et al.* Dictionary learning for integrative, multimodal and scalable single-cell analysis. *Nat Biotechnol* (2023) doi:10.1038/s41587-023-01767-y.

Acknowledgements

This work was supported by the Flow Cytometry Facility and the Sequencing Facility, two core facilities of the Interdisciplinary Center for Clinical Research (IZKF) Aachen within the Faculty of Medicine at RWTH Aachen University. We thank Dr. Mira Jakovcevski, Hendro Langecker, Dorothee Hoffmann, Pia Döring and Ananya Sangeetha for their experimental support, and Sandra Brill for her support with mouse care and genotyping. We further thank Prof. Dr. Christoph Kuppe, Emilia Scheidereit and Vanessa Künstler for the access to and support with MERESCOPE.

Funding

This research was funded by the Deutsche Forschungsgemeinschaft (DFG, German Research Foundation)—368482240/GRK2416, ZI-1224/13-1, ZI-1224/19-1 dedicated to GZB, and 322977937/GRK2344 to C.L.F. and T.V.; the study was further funded under the Excellence Strategy of the Federal Government and the Länder (OPSF678, OPSF812, SFASIA002) dedicated to G.Z.B.; S.X. acknowledges the support of the China Scholarship Council program (Project ID: 202306650006). K.Z. received financial support from the European Union-NextGenerationEU-Project (CUP F53D23001170006).

Author contributions

J.R. performed experiments and data analysis, figure illustration, manuscript editing; P.W. performed experiments and data analysis, figure illustration, manuscript editing; S.X. performed the *in silico* experiments, data analysis, and figure illustration; K.Z. performed the *in silico* experiments and data analysis; C.L.F. performed experiments and data analysis; J.D. performed experiments and data analysis; S.G. performed experiments and data analysis; J.L. performed experiments and data analysis; C.B.Y. performed experiments and data analysis; G.P. performed experiments and data analysis; G.N. methods support and data analysis; L.D. performed experiments and data analysis; J.V. performed experiments and data analysis; L.B. performed experiments and data analysis; S.K. performed experiments and data analysis; M.S. performed experiments and data analysis, K.N.M. Data analysis, data discussion; C.C.K. data analysis; T.V. data discussion and analysis, manuscript editing; P.C. data interpretation

and discussion, wrote the *in silico* analysis; S.M. data analysis and discussion, figure illustration, manuscript preparation; G.Z.B. conceptual design, administration and supervision, experimental design, wrote the manuscript, figure illustration, data analysis, interpretation and discussion.

Competing Interests

None.

Main Figures

Figure 1:

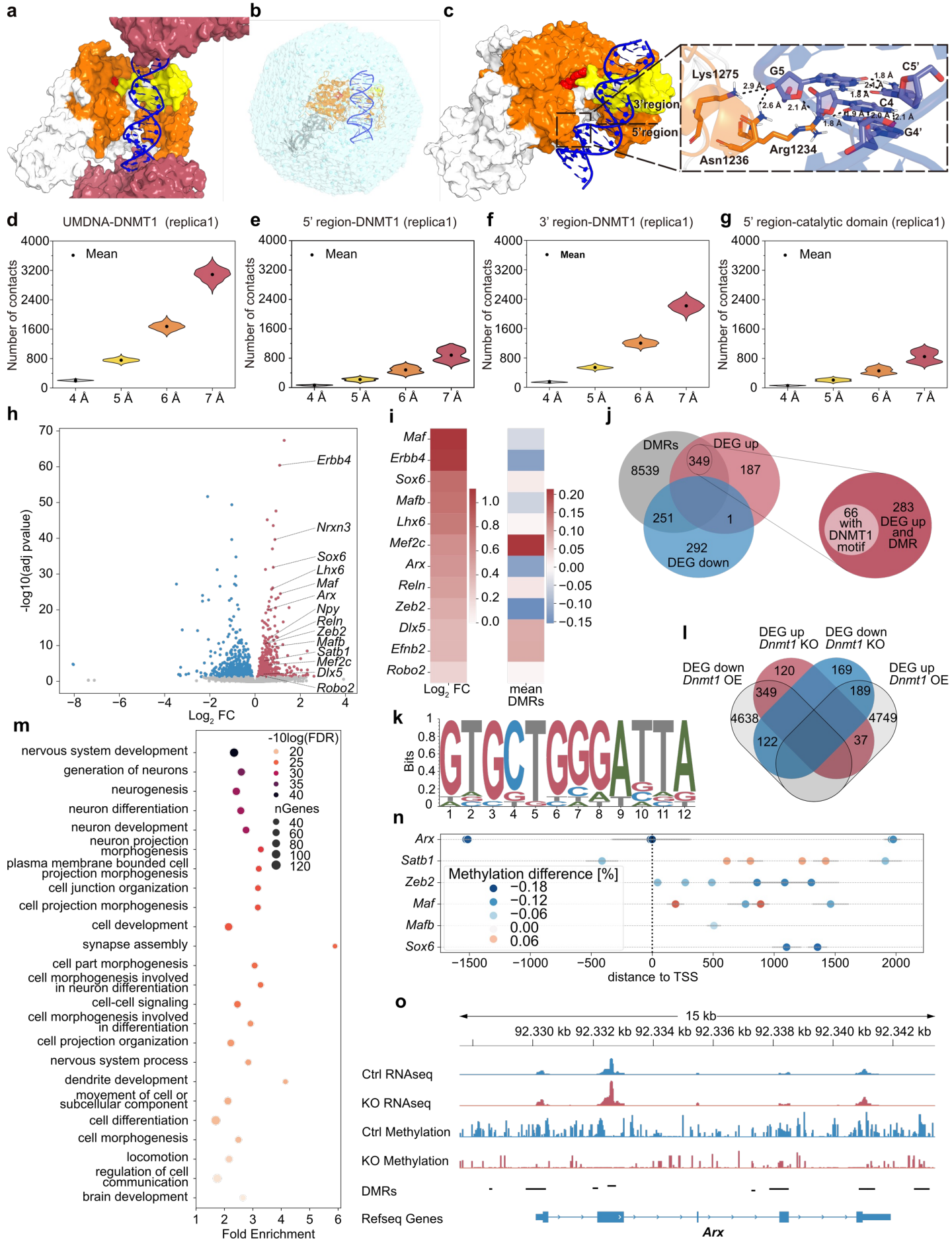
a
b
c
3'region
5'region
Lys1275
G5
C5'
C4
G4'
Arg1234
Asn1236
d UMDNA-DNMT1 (replica1)
e 5' region-DNMT1 (replica1)
f 3' region-DNMT1 (replica1)
g 5' region-catalytic domain (replica1)
Mean
Number of contacts
4 Å
5 Å
6 Å
7 Å
h
-log10(adj pvalue)
Log2 FC
Erbb4
Nrxn3
Sox6
Lhx6
Maf
Arx
Npy
Reln
Zeb2
Mafb
Satb1
Mef2c
Dlx5
Robo2
i
Maf
Erbb4
Sox6
Mafb
Lhx6
Mef2c
Arx
Reln
Zeb2
Dlx5
Efnb2
Robo2
Log2 FC
mean DMRs
j
DMRs
DEG up
8539
349
187
251
1
292 DEG down
66 with DNMT1 motif
283 DEG up and DMR
l
DEG up Dnmt1 KO
DEG down Dnmt1 KO
DEG down Dnmt1 OE
DEG up Dnmt1 OE
120
169
349
189
4638
4749
122
37
k
Bits
m
-10log(FDR)
nGenes
nervous system development
generation of neurons
neurogenesis
neuron differentiation
neuron development
neuron projection morphogenesis
plasma membrane bounded cell projection morphogenesis
cell junction organization
cell projection morphogenesis
cell development
synapse assembly
cell part morphogenesis
cell morphogenesis involved in neuron differentiation
cell-cell signaling
cell morphogenesis involved in differentiation
cell projection organization
nervous system process
dendrite development
movement of cell or subcellular component
cell differentiation
cell morphogenesis
locomotion
regulation of cell communication
brain development
Fold Enrichment
n
Methylation difference [%]
distance to TSS
o
15 kb
92.330 kb 92.332 kb 92.334 kb 92.336 kb 92.338 kb 92.340 kb 92.342 kb
Ctrl RNAseq
KO RNAseq
Ctrl Methylation
KO Methylation
DMRs
Refseq Genes
Arx

Figure 2

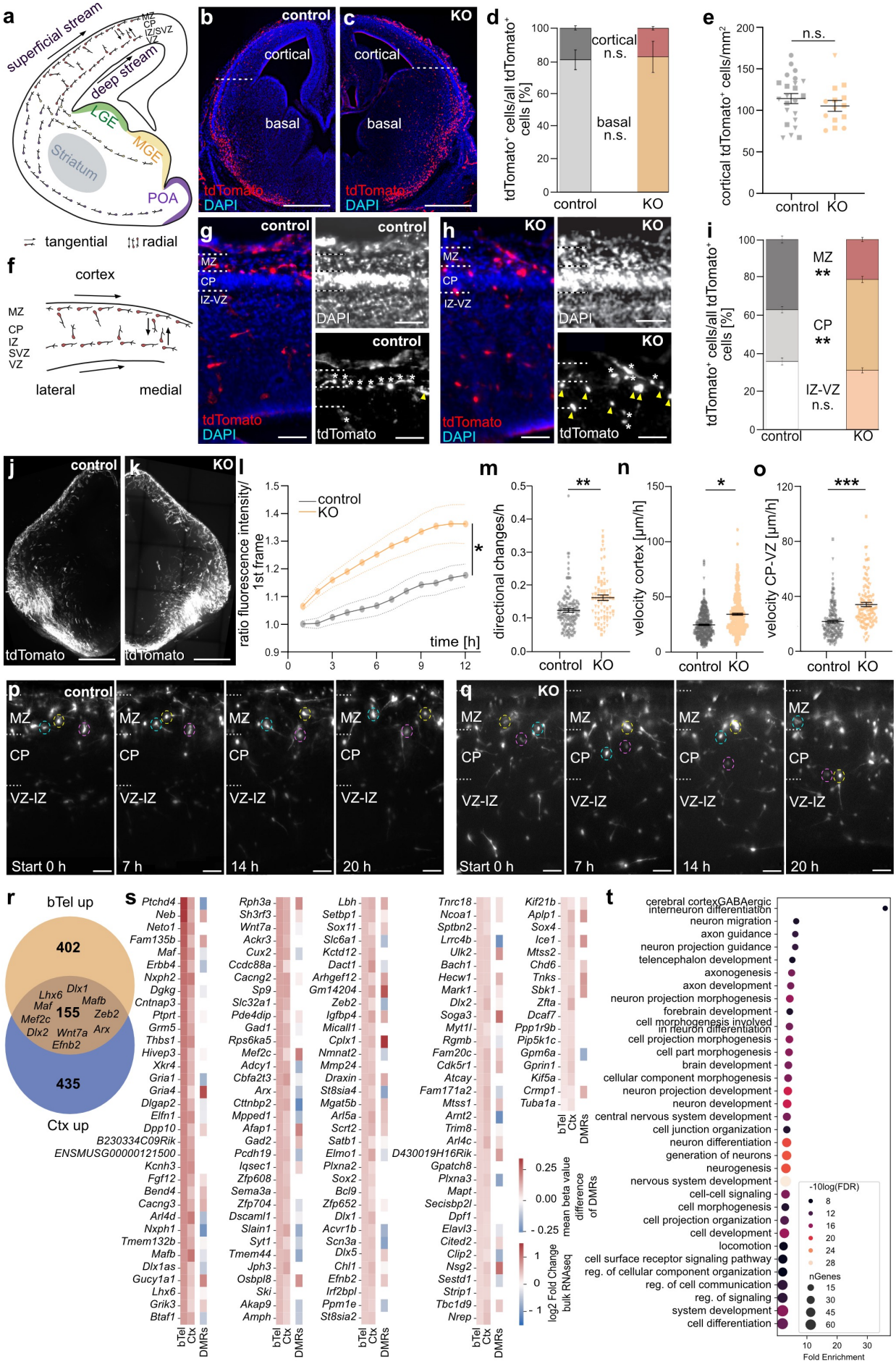
a
superficial stream
deep stream
MZ
CP
IZ/SVZ
VZ
LGE
MGE
Striatum
POA
tangential
radial
b
control
cortical
basal
tdTomato
DAPI
c
KO
cortical
basal
tdTomato
DAPI
d
tdTomato+ cells/all tdTomato+ cells [%]
cortical n.s.
basal n.s.
control
KO
e
cortical tdTomato+ cells/mm2
n.s.
control
KO
f
cortex
MZ
CP
IZ
SVZ
VZ
lateral
medial
g
control
MZ
CP
IZ-VZ
DAPI
tdTomato
h
KO
MZ
CP
IZ-VZ
DAPI
tdTomato
i
tdTomato+ cells/all tdTomato+ cells [%]
MZ **
CP **
IZ-VZ n.s.
control
KO
j
control
tdTomato
k
KO
tdTomato
l
ratio fluorescence intensity/ 1st frame
control
KO
time [h]
m
directional changes/h
**
control
KO
n
velocity cortex [µm/h]
*
control
KO
o
velocity CP-VZ [µm/h]
***
control
KO
p
control
MZ
CP
VZ-IZ
Start 0 h
7 h
14 h
20 h
q
KO
MZ
CP
VZ-IZ
Start 0 h
7 h
14 h
20 h
r
bTel up
402
Lhx6
Dlx1
Maf
Mafb
155
Mef2c
Zeb2
Dlx2
Wnt7a
Arx
Efnb2
435
Ctx up
s
Ptchd4
Neb
Neto1
Fam135b
Maf
Erbb4
Nxph2
Dgkg
Cntnap3
Ptprt
Grm5
Thbs1
Hivep3
Xkr4
Gria1
Gria4
Dlgap2
Elfn1
Dpp10
B230334C09Rik
ENSMUSG00000121500
Kcnh3
Fgf12
Bend4
Cacng3
Arl4d
Nxph1
Tmem132b
Mafb
Dlx1as
Gucy1a1
Lhx6
Grik3
Btaf1
Rph3a
Sh3rf3
Wnt7a
Ackr3
Cux2
Ccdc88a
Cacng2
Sp9
Slc32a1
Pde4dip
Gad1
Rps6ka5
Mef2c
Adcy1
Cbfa2t3
Arx
Cttnbp2
Mpped1
Afap1
Gad2
Pcdh19
Iqsec1
Zfp608
Sema3a
Zfp704
Dscaml1
Slain1
Syt1
Tmem44
Jph3
Osbpl8
Ski
Akap9
Amph
Lbh
Setbp1
Sox11
Slc6a1
Kctd12
Dact1
Arhgef12
Gm14204
Zeb2
Igfbp4
Micall1
Cplx1
Nmnat2
Mmp24
Draxin
St8sia4
Mgat5b
Arl5a
Scrt2
Satb1
Elmo1
Plxna2
Sox2
Bcl9
Zfp652
Dlx1
Acvr1b
Scn3a
Dlx5
Chl1
Efnb2
Irf2bpl
Ppm1e
St8sia2
Tnrc18
Ncoa1
Sptbn2
Lrrc4b
Ulk2
Bach1
Hecw1
Mark1
Dlx2
Soga3
Myt1l
Rgmb
Fam20c
Cdk5r1
Atcay
Fam171a2
Mtss1
Arnt2
Trim8
Arl4c
D430019H16Rik
Gpatch8
Plxna3
Mapt
Secisbp2l
Dpf1
Elavl3
Cited2
Clip2
Nsg2
Sestd1
Strip1
Tbc1d9
Nrep
Kif21b
Aplp1
Sox4
Ice1
Mtss2
Chd6
Tnks
Sbk1
Zfta
Dcaf7
Ppp1r9b
Pip5k1c
Gpm6a
Gprin1
Kif5a
Crmp1
Tuba1a
bTel
Ctx
DMRs
mean beta value difference of DMRs
0.25
0.00
- 0.25
log2 Fold Change bulk RNAseq
1
0
- 1
t
cerebral cortexGABAergic interneuron differentiation
neuron migration
axon guidance
neuron projection guidance
telencephalon development
axonogenesis
axon development
neuron projection morphogenesis
forebrain development
cell morphogenesis involved in neuron differentiation
cell projection morphogenesis
cell part morphogenesis
brain development
cellular component morphogenesis
neuron projection development
neuron development
central nervous system development
cell junction organization
neuron differentiation
generation of neurons
neurogenesis
nervous system development
cell-cell signaling
cell morphogenesis
cell projection organization
cell development
locomotion
cell surface receptor signaling pathway
reg. of cellular component organization
reg. of cell communication
reg. of signaling
system development
cell differentiation
-10log(FDR)
8
12
16
20
24
28
nGenes
15
30
45
60
10
20
30
Fold Enrichment

Figure 3

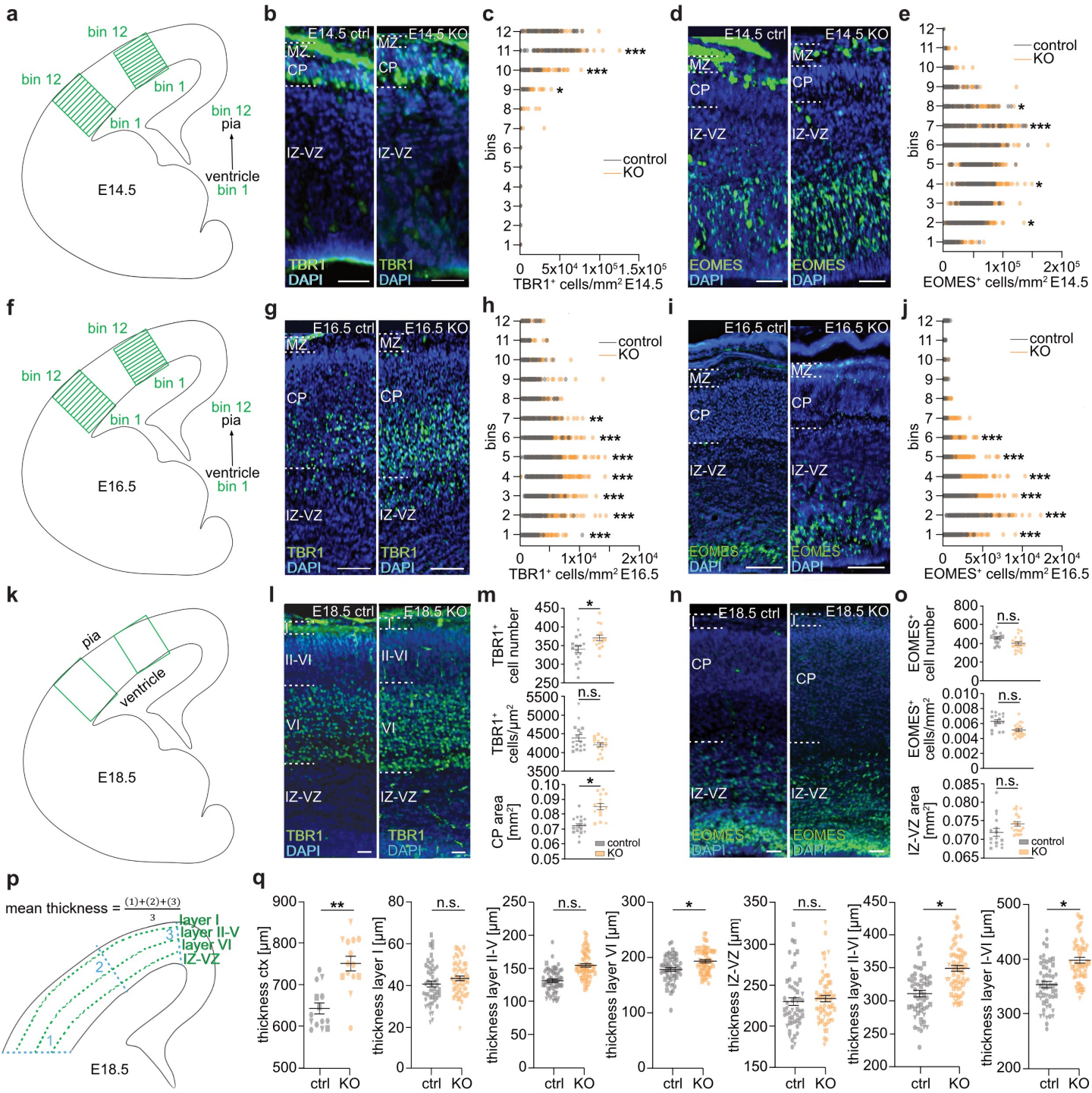
a
bin 12
bin 12
bin 1
bin 1
bin 12
pia
ventricle
bin 1
E14.5
b
E14.5 ctrl
E14.5 KO
MZ
CP
IZ-VZ
TBR1
DAPI
c
bins
control
KO
TBR1⁺ cells/mm² E14.5
d
E14.5 ctrl
E14.5 KO
EOMES
DAPI
e
control
KO
bins
EOMES⁺ cells/mm² E14.5
f
E16.5
g
E16.5 ctrl
E16.5 KO
h
TBR1⁺ cells/mm² E16.5
i
j
EOMES⁺ cells/mm² E16.5
k
pia
ventricle
E18.5
l
E18.5 ctrl
E18.5 KO
II-VI
VI
m
TBR1⁺ cell number
TBR1⁺ cells/µm²
CP area [mm²]
n.s.
n
o
EOMES⁺ cell number
EOMES⁺ cells/mm²
IZ-VZ area [mm²]
p
mean thickness = (1)+(2)+(3) / 3
layer I
layer II-V
layer VI
IZ-VZ
E18.5
q
thickness ctx [µm]
thickness layer I [µm]
thickness layer II-V [µm]
thickness layer VI [µm]
thickness IZ-VZ [µm]
thickness layer II-VI [µm]
thickness layer I-VI [µm]
ctrl
KO

Figure 4

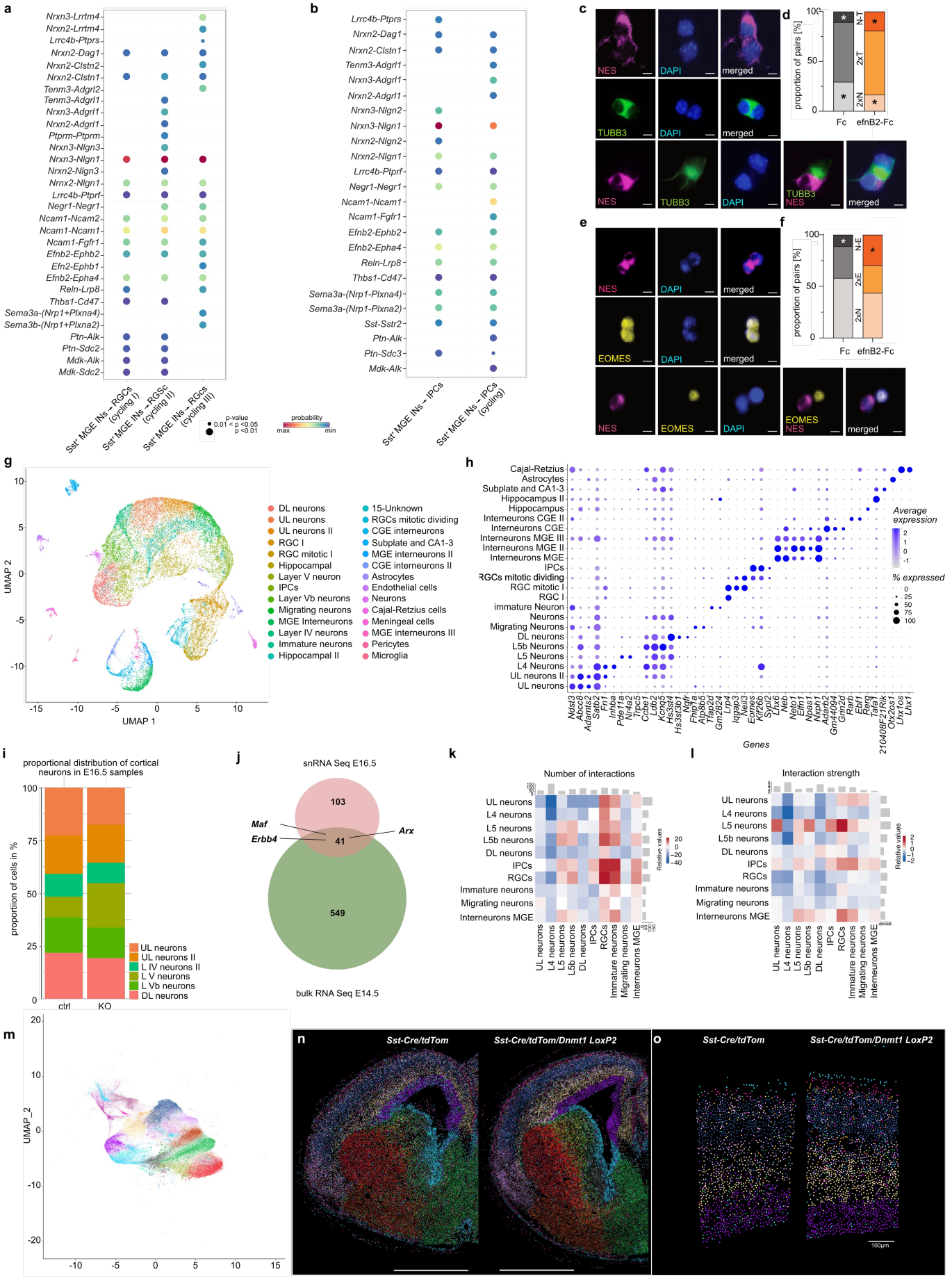
a
Nrxn3-Lrrtm4
Nrxn2-Lrrtm4
Lrrc4b-Ptprs
Nrxn2-Dag1
Nrxn2-Clstn2
Nrxn2-Clstn1
Tenm3-Adgrl2
Tenm3-Adgrl1
Nrxn3-Adgrl1
Nrxn2-Adgrl1
Ptprm-Ptprm
Nrxn3-Nlgn3
Nrxn3-Nlgn1
Nrxn2-Nlgn3
Nrnx2-Nlgn1
Lrrc4b-Ptprf
Negr1-Negr1
Ncam1-Ncam2
Ncam1-Ncam1
Ncam1-Fgfr1
Efnb2-Ephb2
Efn2-Ephb1
Efnb2-Epha4
Reln-Lrp8
Thbs1-Cd47
Sema3a-(Nrp1+Plxna4)
Sema3b-(Nrp1+Plxna2)
Ptn-Alk
Ptn-Sdc2
Mdk-Alk
Mdk-Sdc2
Sst+ MGE INs ~ RGCs (cycling I)
Sst+ MGE INs ~ RGSc (cycling II)
Sst+ MGE INs ~ RGcs (cycling III)
p-value
0.01 < p <0.05
p <0.01
probability
max
min
b
Lrrc4b-Ptprs
Nrxn2-Dag1
Nrxn2-Clstn1
Tenm3-Adgrl1
Nrxn3-Adgrl1
Nrxn2-Adgrl1
Nrxn3-Nlgn2
Nrxn3-Nlgn1
Nrxn2-Nlgn2
Nrxn2-Nlgn1
Lrrc4b-Ptprf
Negr1-Negr1
Ncam1-Ncam1
Ncam1-Fgfr1
Efnb2-Ephb2
Efnb2-Epha4
Reln-Lrp8
Thbs1-Cd47
Sema3a-(Nrp1-Plxna4)
Sema3a-(Nrp1-Plxna2)
Sst-Sstr2
Ptn-Alk
Ptn-Sdc3
Mdk-Alk
Sst+ MGE INs ~ IPCs
Sst+ MGE INs ~ IPCs (cycling)
c
NES
DAPI
merged
TUBB3
d
proportion of pairs [%]
N-T
2xT
2xN
Fc
efnB2-Fc
e
EOMES
f
N-E
2xE
g
UMAP 1
UMAP 2
DL neurons
UL neurons
UL neurons II
RGC I
RGC mitotic I
Hippocampal
Layer V neuron
IPCs
Layer Vb neurons
Migrating neurons
MGE Interneurons
Layer IV neurons
Immature neurons
Hippocampal II
15-Unknown
RGCs mitotic dividing
CGE interneurons
Subplate and CA1-3
MGE interneurons II
CGE interneurons II
Astrocytes
Endothelial cells
Neurons
Cajal-Retzius cells
Meningeal cells
MGE interneurons III
Pericytes
Microglia
h
Cajal-Retzius
Astrocytes
Subplate and CA1-3
Hippocampus II
Hippocampus
Interneurons CGE II
Interneurons CGE
Interneurons MGE III
Interneurons MGE II
Interneurons MGE
IPCs
RGCs mitotic dividing
RGC mitotic I
RGC I
immature Neuron
Neurons
Migrating Neurons
DL neurons
L5b Neurons
L5 Neurons
L4 Neurons
UL neurons II
UL neurons
Average expression
% expressed
Genes
i
proportional distribution of cortical neurons in E16.5 samples
proportion of cells in %
ctrl
KO
UL neurons
UL neurons II
L IV neurons II
L V neurons
L Vb neurons
DL neurons
j
snRNA Seq E16.5
103
Maf
Erbb4
41
Arx
549
bulk RNA Seq E14.5
k
Number of interactions
Relative values
l
Interaction strength
m
UMAP_1
UMAP_2
n
Sst-Cre/tdTom
Sst-Cre/tdTom/Dnmt1 LoxP2
o
100µm
p
Developing medium spiny neuron precursors
Medium spiny neuron precursors
Medium spiny neuron precursors
Astrocyte Precursors
OPCs
Microglia
Endothelial Cells and Pericytes
Cajal-Retzius-cells
Dividing GABAergic progenitors
Dividing IN progenitors
cIN precursors (Lhx6+)
Migrating GABAergic interneurons
Developing SST+ interneurons
RGCs
NPCs
Dividing cortical neural progenitors
IPCs
Dividing IPCs
Undefined Dividing Neural Progenitors
Developing cortical neurons
Developing cortical projection neurons
Developing DL cortical neurons
DL cortical neurons

Figure 5

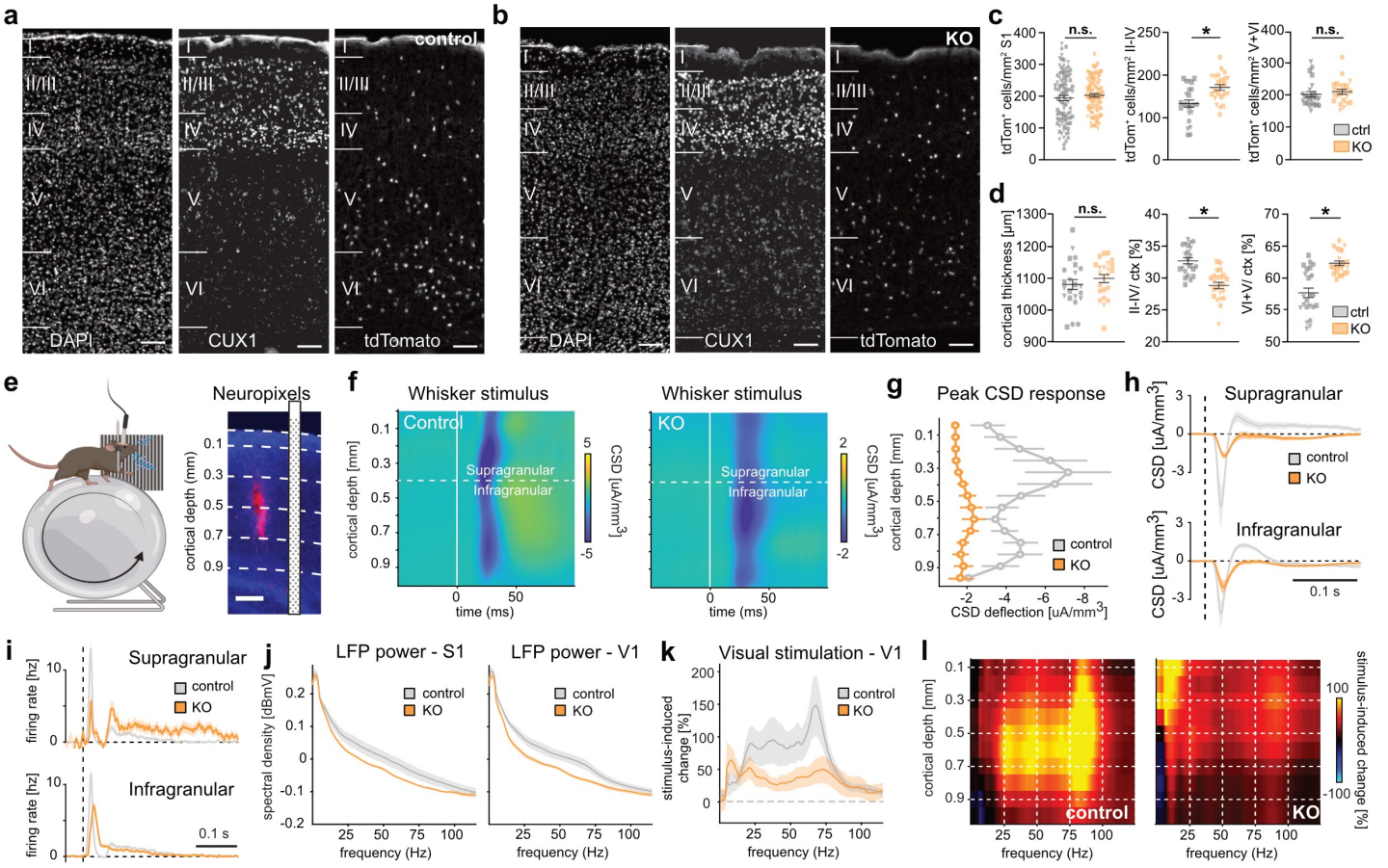
a
control
I
II/III
IV
V
VI
DAPI
CUX1
tdTomato
b
KO
c
tdTom+ cells/mm² S1
tdTom+ cells/mm² II-IV
tdTom+ cells/mm² V+VI
n.s.
*
ctrl
KO
d
cortical thickness [µm]
II-IV/ ctx [%]
VI+V/ ctx [%]
e
Neuropixels
cortical depth (mm)
f
Whisker stimulus
Control
KO
Supragranular
Infragranular
CSD [uA/mm3]
time (ms)
g
Peak CSD response
cortical depth [mm]
CSD deflection [uA/mm3]
h
Supragranular
Infragranular
CSD [uA/mm3]
0.1 s
i
Supragranular
Infragranular
firing rate [hz]
j
LFP power - S1
LFP power - V1
spectral density [dBmV]
frequency (Hz)
k
Visual stimulation - V1
stimulus-induced change [%]
l
stimulus-induced change [%]

Figure 6

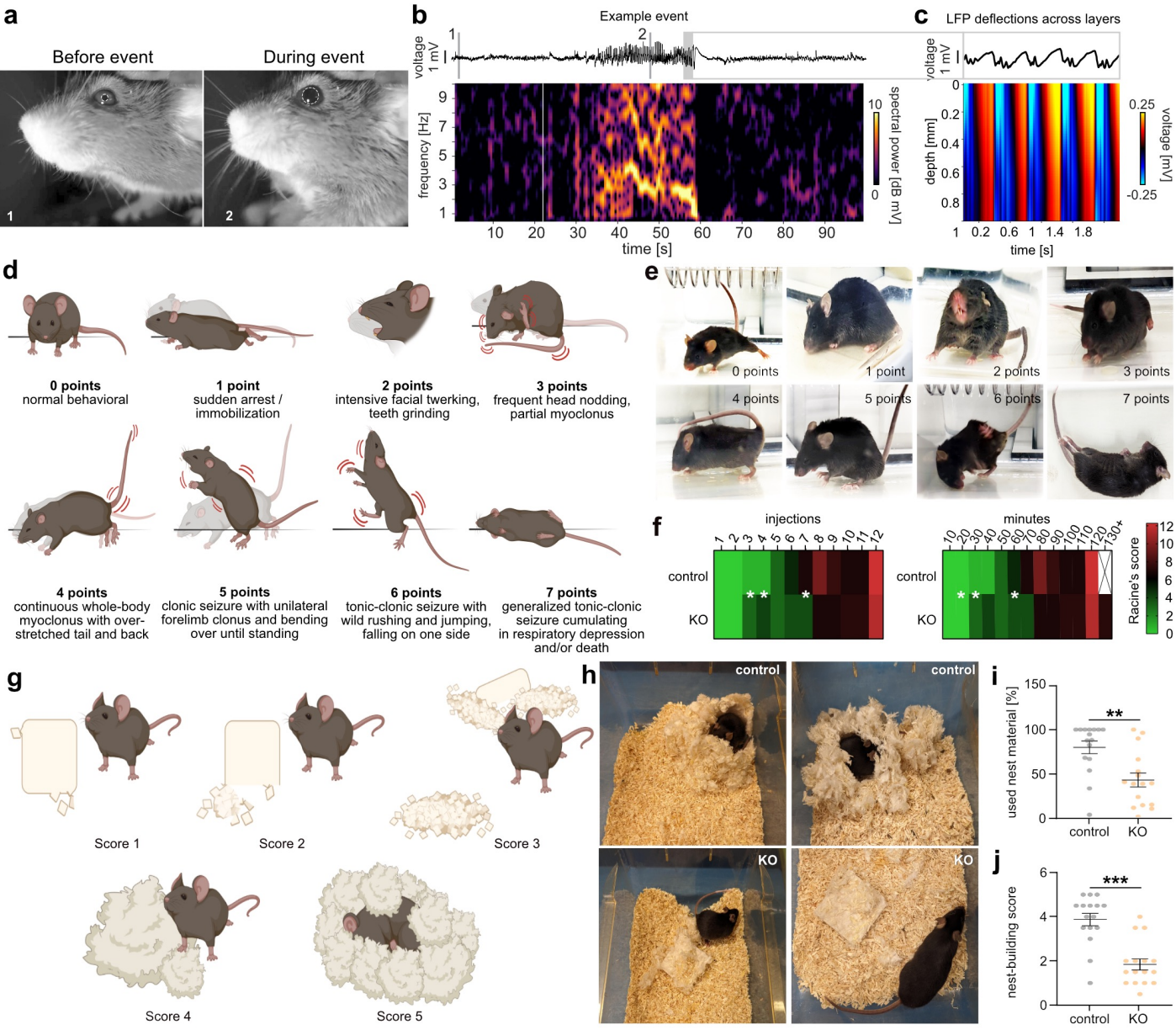
a
Before event
During event
b
Example event
voltage
1 mV
frequency [Hz]
spectral power [dB mV]
time [s]
c
LFP deflections across layers
depth [mm]
voltage [mV]
time [s]
d
0 points
normal behavioral
1 point
sudden arrest / immobilization
2 points
intensive facial twerking, teeth grinding
3 points
frequent head nodding, partial myoclonus
4 points
continuous whole-body myoclonus with over-stretched tail and back
5 points
clonic seizure with unilateral forelimb clonus and bending over until standing
6 points
tonic-clonic seizure with wild rushing and jumping, falling on one side
7 points
generalized tonic-clonic seizure cumulating in respiratory depression and/or death
e
0 points
1 point
2 points
3 points
4 points
5 points
6 points
7 points
f
injections
minutes
control
KO
Racine's score
g
Score 1
Score 2
Score 3
Score 4
Score 5
h
control
control
KO
KO
i
used nest material [%]
control
KO
j
nest-building score
control
KO